Optical Properties and Biological Applications of Fluorescent Gold Nano-clusters

Thesis for Mphil's degree

Han Zhou

12/07/2015

Department of Physics

University of Strathclyde

Declaration of Authenticity and Author's Rights

This thesis is the result of the author’s original research. It has been composed by the author and has not been previously submitted for examination which has led to the award of a degree.

Signed: Han Zhou

Date: 12 July 2015

Abstract

As a novel fluorescent nanomaterial, fluorescent gold nanoclusters (AuNCs) possess numerous exceptional characteristics compared with other luminescent materials such as good water-solubility, high photostability, large Stokes shift, ultrasmall size, nontoxicity, and good biocompatibility.

Despite promising applications and intensive interests, the study of the fluorescence mechanism of AuNCs has so far been limited. In order to investigate the factors that determine the fluorescence properties of Bovine Serum Albumin (BSA) encapsulated AuNCs (BSA-AuNCs), the influence of pH during nanocluster growth on the fluorescence properties of AuNCs has been studied. Both fluorescence emission and lifetime were found to be affected by synthetic pH, and such an effect could not be reversed even if the pH changed after the synthesis.

Biological applications of AuNCs have also been studied in order to explore the potential application in biosensing and bioimaging. Fluorescence anisotropy spectroscopic study confirmed the bio-chemical activities of BSA in BSA-AuNCs, demonstrating a new possibility of using BSA-AuNCs as fluorescence probe. And the bioimaging study of BSA-AuNC in intestine sections of a mouse that was fed by oral gavages opens a new way for using AuNCs on pharmaceutical and biological studies.

Contents

1. Introduction

1.1 Fluorescence

Fluorescence is a form of photoluminescence which describes the process of the emission of light by a substance that has absorbed photons (electromagnetic radiation).[1] As a consequence of being a spin-allowed singlet-singlet transition process, fluorescence has a much higher quantum yield and is usually easier to study than the other form of photoluminescence, phosphorescence, which involves a spin-forbidden triplet-singlet transition.

The processes of photoluminescence which include the absorption and emission of light could be described by the Jablonski diagrams named after Professor Alexander Jablonski. Jablonski diagrams have various forms to represent different kinds of processes of excitation and emission. Figure 1.1 shows a typical Jablonski diagram which illustrates the fluorescence process as well as the phosphorescence process.

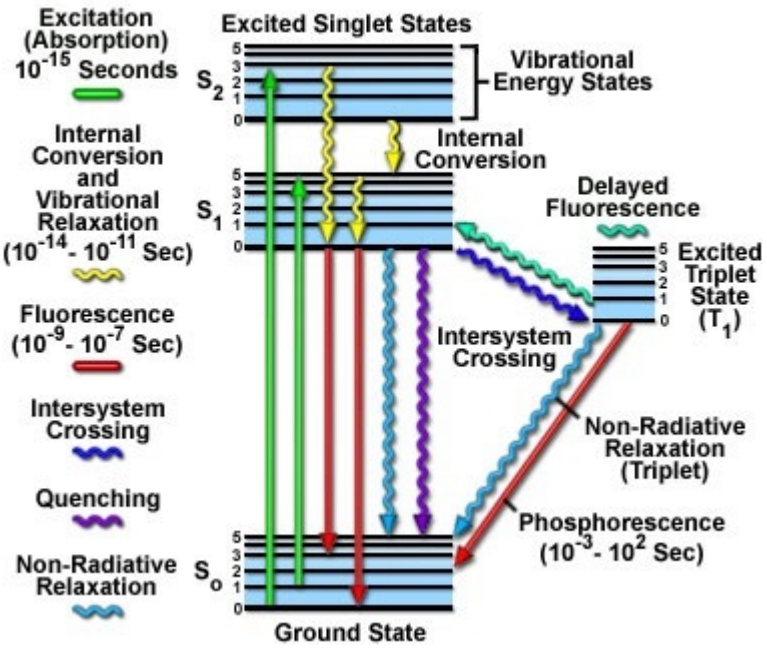

Figure 1.1 Jablonski diagram illustrates the photoluminescence process.
figure from http://micro.magnet.fsu.edu/primer/java/jablonski/lightandcolor/index.html

In Figure 1.1, the green arrows used to indicate excitation (absorption) are longer than the red arrows used to indicate emission, which indicates that the emission photon energy is usually lower than the excitation photon mostly due to the yellow process known as internal conversion and vibrational relaxation where electromagnetic energy becomes heat. In the macroscopic view, the wavelength of the emission light would be longer than the excitation; this phenomenon is known as Stokes shift which was first observed by Sir G. G. Stokes in 1852.

Among the red straight arrows used for emission, the two vertical arrows represent fluorescence whereas the inclined one indicates phosphorescence. In the fluorescence process, the excited electron has the opposite spin to the second electron in the ground state, and thus, transition to the ground state is spin allowed and happens rather quickly by emitting a photon. A typical fluorescence lifetime (which will be explained in detail later) means the average time the molecule spends in the excited state before returning to the ground state is in the range of nanoseconds.

As shown in figure 1.1, during the process of phosphorescence, an emission photon would be generated as the electron which transfers originally from the excited singlet states through intersystem crossing (blue arrow in figure 1.1, no photon is involved in this process) jumped from the excited triplet states to the ground state: the electron in the excited states has the same spin as the ground state electron, and, as a consequence, returning to the ground state is spin forbidden and takes much more time than fluorescence. The lifetime of phosphorescence is usually between several milliseconds to several seconds, or even longer.

There’s also a special kind of fluorescence known as delayed fluorescence which process a lifetime as longs as several microseconds. This happens when an electron on excited triplet states ‘decides’ to go back to excited singlet states instead of jump directly to ground states. No photon is involved in this whole process besides the absorption and emission as normal fluorescence; however, the lifetime would be prolonged by a factor of thousands. This kind of fluorescence is mostly observed in noble metal quantum dots which are also known as nanoclusters.

Not all the excited electrons would emit photons as they transfer from excited states to ground states. The light blue arrows in figure 1.1 shows nonradioactive relaxation where electromagnetic energy becomes other kinds of energy without the emission of light. The number of emitted photons relative to the number of absorbed photons is defined as quantum yield. The higher the quantum yield is (approaching to a maximum of one), the brighter the fluorescence emission would be.

Quantum yield could be reduced by a wide variety of processes; such decrease in intensity is called fluorescence quenching which is shown in figure 1.1 as a purple arrow. Quenching can occur by different mechanisms which include excited-state reactions, molecular rearrangements, energy transfer, ground-state complex formation, and collision quenching.

The use of fluorescence within biological science has been expanded during the last decades: besides its use in biochemistry and biophysics with steady state fluorescence spectroscopy and time-resolved fluorescence spectroscopy, fluorescence is now a dominant technique used extensively in biotechnology, including flow cytometry DNA sequencing and genetic analysis, as well as in medical diagnostics, forensics, etc. Fluorescence probes have replaced radioactive tracers in many biochemical measurements because of the remarkable development of fluorescence detection and its high sensitivity and relatively low cost.

1.1.1 Absorption and Fluorescence

Absorption and fluorescence spectroscopy provide essential information on the optical properties of fluorophores which could be used to identify the fluorophores or their electronic status. Although more advanced implements such as time-resolved fluorescence measurement or fluorescence anisotropy have been applied, steady state fluorescence spectroscopy still plays a vital role in fluorescence study.

As a function of frequency or wavelength, absorption spectrum is used to represent the fluorophores' ability to absorb radiation of certain wavelength (Blue arrows in figure

1.2(a)), whereas fluorescence spectrum indicates the fluorophores' photoluminescence properties under certain excitation light (Red arrows in figure 1.2(b)).

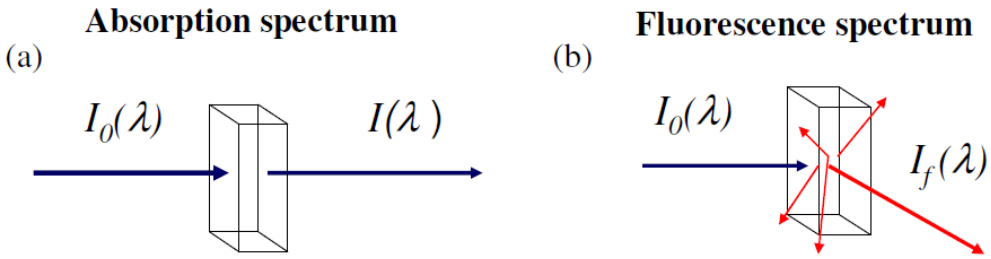

Figure 1.2 Measurement of (a) absorption spectrum and (b) fluorescence spectrum[1]

Figure 1.2 illustrates how absorption and fluorescence spectra are measured: in absorption spectra, the transmitted light should always be detected in-line as the incident light, whereas fluorescence is usually detected off-axis to avoid the penetrated incident light which would otherwise swamp the much smaller fluorescence signal. Generally, fluorescence is isotropic and is usually detected at 90° to the excitation as figure 1.2 (b) showed and a light filter should also be applied to eliminate the excitation's scattering.

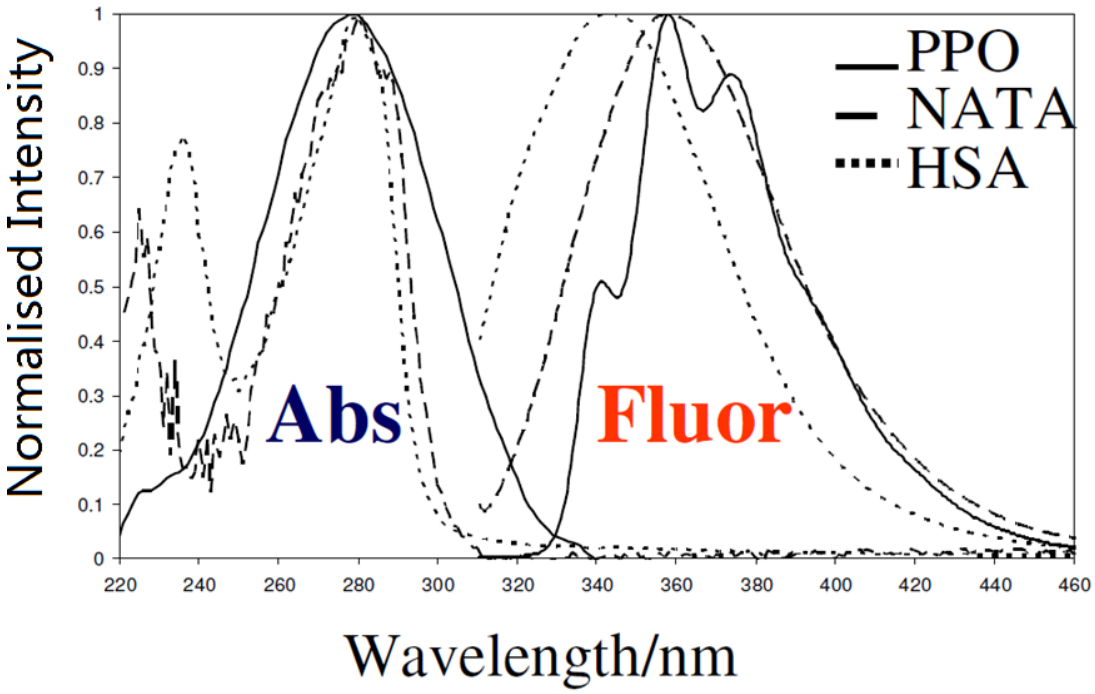

Figure 1.3 Absorption and fluorescence spectra measured in condensed media. PPO refers to the scintillator 2,5-diphenyloxazole, NATA is N-acetyl-L-tryptophanamide, a derivative of the fluorescent amino acid tryptophan and HSA the protein Human Serum Albumin which contains a single tryptophan[1]**.**

Figure 1.3 illustrates the absorption and fluorescence spectra of three different kinds of fluorophores. As mentioned before, the phenomenon known as Stokes shift is observed here where the emission photon has a longer wavelength than the absorption. Energy losses between excitation and emission are common among fluorescence molecules in solution due to internal conversion and vibrational relaxation, solvent effect (polarized molecule orientation), excited-state reactions, complex formations, and energy transfer.

Another general property of fluorescence is that the same fluorescence emission spectrum is generally observed irrespective of the excitation wavelength. This is known as Kasha's rule. This phenomenon is caused by the rapid relaxation of excited fluorophore: when the electron is excited into higher electronic and vibrational levels, it would quickly drop to the lowest vibrational level (in about 1ps) and dissipate the excess energy which is supposed to be the consequence of a strong overlap among numerous states of nearly equal energy. There are fluorophores that do not obey this rule; however such fluorophores are rare and generally not seen in biological molecules.

1.1.2 Fluorescence Quantum Yield and Lifetime

As mentioned before, the number of emitted photons relative to the number of absorbed photons is defined as fluorescence quantum yield which could provide us with information on the fluorophores' optical properties.

Besides fluorescence wavelength and quantum yield, fluorescence lifetime is also a very important characteristic which could be used to identify fluorophores and describe the fluorescence process. Time-resolved measurement has emerged recently as the most powerful and versatile technique in fluorescence spectroscopy. Compared to steady state fluorescence spectroscopy, fluorescence lifetime study provides more kinetic information which could be easily interpreted and calibrated. Lifetime measurement could also be incorporated in fluorescence microscopy, e.g., fluorescence lifetime imaging microscopy (FLIM).

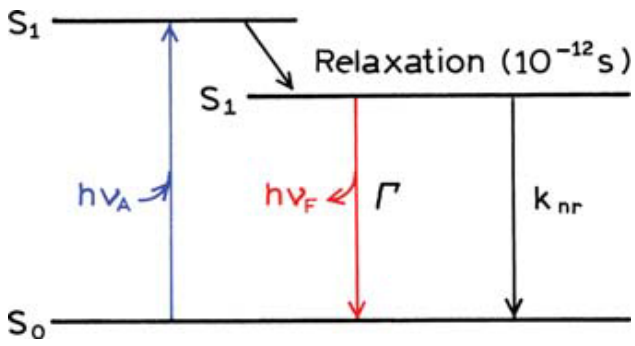

Figure 1.4 A simplified Jablonski diagram to illustrate the meaning of quantum yields and lifetimes[1]

The concept of quantum yield and lifetime can be easily illustrated with a simplified Jablonski diagram (figure 1.4). Here we use the emissive rate of the fluorophore (Γ) and its rate of nonradiative decay (k_{nr}) to describe the fluorescence quantum yield.

$$Q = \frac{\Gamma}{\Gamma + k_{nr}} \tag{1.1}$$

The quantum yield can be close to unity if the radiative decay is much larger than the nonradiative decay.

The lifetime of the excited state is defined as the average time the excited electron spends in the excited states before it jumps back to the ground state. The lifetime in figure 1.4 should be

$$\tau = \frac{1}{\Gamma + k_{nr}} \tag{1.2}$$

Fluorescence is a random process, and few molecules emit photons according to the lifetime. The lifetime is an average value of the time spent in the excited states. Figure 1.5 shows an example of fluorescence decay obtained through time-correlated single photon counting (TCSPC) technique on a logarithmic scale.

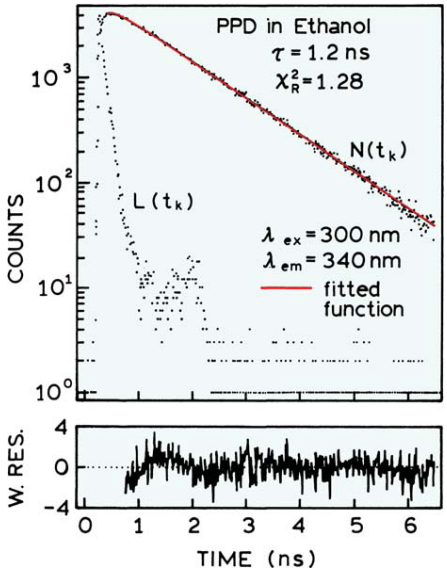

Figure 1.5 TCSPC data for 2,5-diphenyl-1,3,4-oxadiazole (PPD) in ethanol. The light source was an R6G dye laser, cavity dumped at 1 MHz. The detector was an R2809 MCP PMT (Hamamatsu). The left side of the residuals (lower panel) show some minor systematic error. [1]

The decay shown in Figure 1.5 is a single exponential decay that follows the equation

$$I = I_0 e^{-t/\tau} \tag{1.3}$$

In this decay, the lifetime is at the time when the fluorescence emission intensity drops to 1/e of the initial emission intensity, and 63% of the molecules have emitted photons before the lifetime and 37% after.

1.1.3 Fluorescence Quenching

Fluorescence intensity can be reduced by a wide variety of processes; such decrease in intensity is called fluorescence quenching. Quenching can occur by different mechanisms which include excited-state reactions, molecular rearrangements, energy transfer, ground-state complex formation, and collisional quenching.

Fluorescence quenching has been widely studied both as a fundamental phenomenon, and as a source of information about biochemical systems. These biochemical applications are based on quenching processes introduced by molecular interactions.

Usually the quenching process requires molecular contact between the fluorophore and quencher.

In the case of collisional quenching, the quencher must diffuse to the fluorophore during the lifetime of the excited state. Upon contact, the fluorophore returns to the ground state, without emission of a photon (Figure 1.6). Quenching occurs without any permanent change in the molecules, that is, the molecules are not chemically altered in the process.

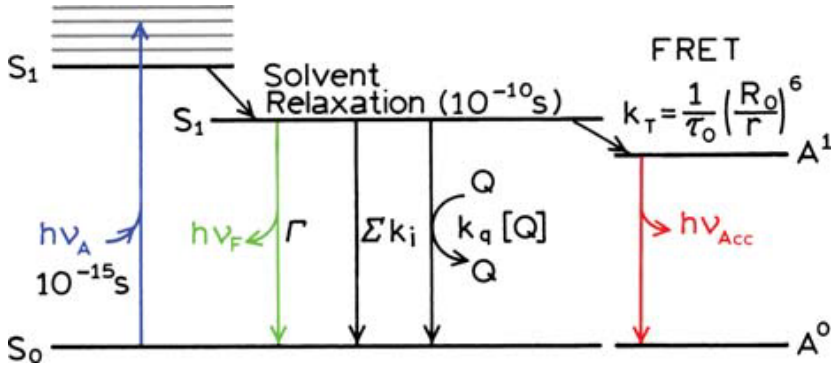

Figure 1.6 Jablonski diagram with collisional quenching and fluorescence resonance energy transfer (FRET)[1]

Collisional quenching of fluorescence is described by the Stern-Volmer equation:

$$\frac{F_0}{F} = 1 + K[Q] = 1 + k_q \tau_0 [Q] \qquad (1.4)$$

In this equation, F_0 and F are the fluorescence intensities in the absence and presence of quencher, respectively; k_q is the bimolecular quenching constant; τ_0 is the lifetime of the fluorophore in the absence of quencher, and Q is the concentration of quencher. The Stern-Volmer quenching constant is given by $K = k_q\tau_0$.

Another important process that occurs in the excited state is fluorescence resonance energy transfer (FRET). This process occurs when the emission spectrum of a fluorophore, called the donor, overlaps with the absorption spectrum of another molecule, called the acceptor, and both donor and acceptor are in a close vicinity to each other. The acceptor does not have to be fluorescent. The FRET process is not a result of the emitted photon from the donor being absorbed by the accepter; it is actually a dipole- dipole interaction between the coupled donor and accepter, and no emission of photons are involved in the process.

The rate of energy transfer depends upon the extent of spectral overlap of the emission spectrum of the donor with the absorption spectrum of the acceptor, the quantum yield of the donor, the relative orientation of the donor and acceptor transition dipoles, and the distance between the donor and acceptor molecules. For convenience the spectral overlap is described in terms of the Förster distance (R_0). The rate of energy transfer $k_T(r)$ is given by

$$k_T(r) = \frac{1}{\tau_D}\left(\frac{R_0}{r}\right)^6 \tag{1.5}$$

where r is the distance between the donor and acceptor, τ_D is the lifetime of the donor in the absence of energy transfer, and R_0 is Förster distance. At R_0, half of the donor molecules decay by energy transfer. R_0 can be calculated using the equation below,

$$R_0^6 = \frac{9000 Q_0 (\ln 10) \kappa^2 J}{128 \pi^5 n^4 N_A} \tag{1.6}$$

where Q_0 is the fluorescence quantum yield of the donor in the absence of the acceptor, κ^2 is the dipole orientation factor, n is the refractive index of the medium, N_A is Avogadro's number, and J is the spectral overlap integral calculated as

$$J = \int f_d(\lambda) \varepsilon_A(\lambda) \lambda^4 d\lambda \tag{1.7}$$

where f_d is the normalized donor emission spectrum, and ε_A is the acceptor molar extinction coefficient.

As the extent of transfer depends on distance, and the Förster distances are comparable in size to biological macromolecules: 3 to 6 nm, FRET could be used as a "spectroscopic ruler" for measuring the separation between acceptors and donors and has become an important tool in, e.g., medical diagnostics, DNA analysis, and optical imaging.

1.1.4 Fluorescence Anisotropy

Upon excitation with polarized light the emission from many fluorophores is also polarized. The extent of polarization of the emission is described in terms of the anisotropy:

$$r = \frac{I_{\parallel} - I_{\perp}}{I_{\parallel} + 2I_{\perp}} \tag{1.8}$$

In this equation, $I_{\parallel}$ represents the observed intensity when emission polarizer is oriented parallel to the direction of the polarized excitation; likewise, when the polarizer is perpendicular to the excitation the intensity is $I_{\perp}$.

Anisotropy measurement is commonly used in the biochemical applications of fluorescence. Anisotropy measurement provides information on the size and shape of fluorophores or rigidity of various molecular environments. Molecular interactions like protein-protein associations could also be studied by anisotropy measurement.

The reason for fluorescence anisotropy is photoselective excitation of fluorophores by polarized light. Fluorophores preferentially absorb photons whose electric vectors are aligned parallel to the transition moment of the fluorophore. The transition moment has a defined orientation with respect to the molecular axis. In a homogeneous solution, the ground-state fluorophores are oriented randomly. When excited with polarized light, those fluorophores that have their absorption transition moments oriented along the electric vector of the incident light are preferentially excited (Figure 1.7). This selective excitation results in a partially oriented population of fluorophores (photoselection), and in partially polarized fluorescence emission. Emission also occurs with the light polarized along a fixed axis in the fluorophore.

The emission can become depolarized by a number of processes, among which the most common cause is rotational diffusion which changes the direction of the transition moments (Figure 1.7). Anisotropy measurements reveal the average angular displacement of the fluorophore that occurs between absorption and subsequent emission of a photon. This angular displacement depends on the rate and extent of

rotational diffusion during the fluorescence lifetime. The rate and extent of rotational diffusion is dependent upon the viscosity of the solvent and the size and shape of the rotating fluorophore. Typically, the rate and extent of rotational diffusion of small fluorophores in low-viscosity solutions is faster than that of large fluorophores in high-viscosity solution. The mechanism would be explained later.

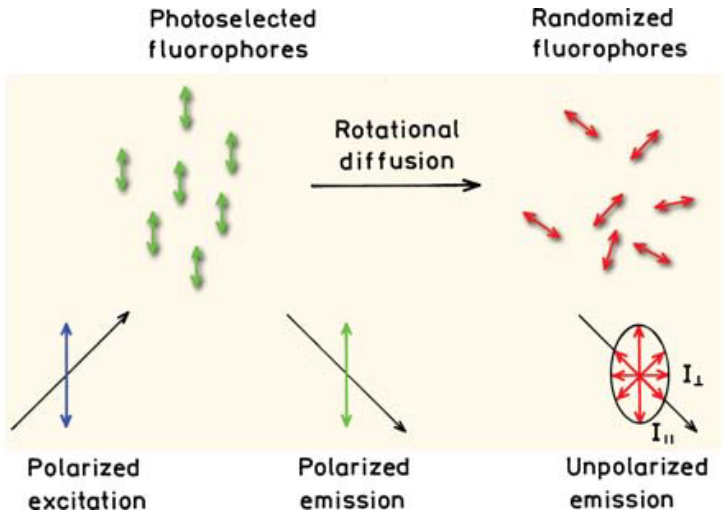

Figure 1.7 Effects of Polarized excitation and rotational diffusion on the emission[1]

Actually, when a sample is illuminated with polarized light, the electric dipole of a fluorophore need not be precisely aligned with the z-axis to absorb light polarized among this axis. However molecules with absorption transitions aligned parallel to the electric vector of the polarized excitation have the highest probability of excitation. The probability of absorption is proportional to $\cos^2 \theta$, where θ is the angle the absorption dipole makes with the z-axis. Hence, excitation with polarized light results in a population of excited fluorophores that are partially oriented along the z-axis (Figure 1.8 (a)). The excited-state population is symmetrical around the z-axis. Most of the excited fluorophores are aligned close to the z-axis, and very few fluorophores have their transition moments oriented in the x-y plane. For the random ground state distribution, which must exist in a disordered solution, the number of molecules at an angle between θ and $\theta + d\theta$ is proportional to $\sin\theta\, d\theta$. Hence, the distribution of molecules excited by vertically polarized light is given by:

$$f(\theta)d\theta = cos^2\theta \sin\theta d\theta \qquad (1.9)$$

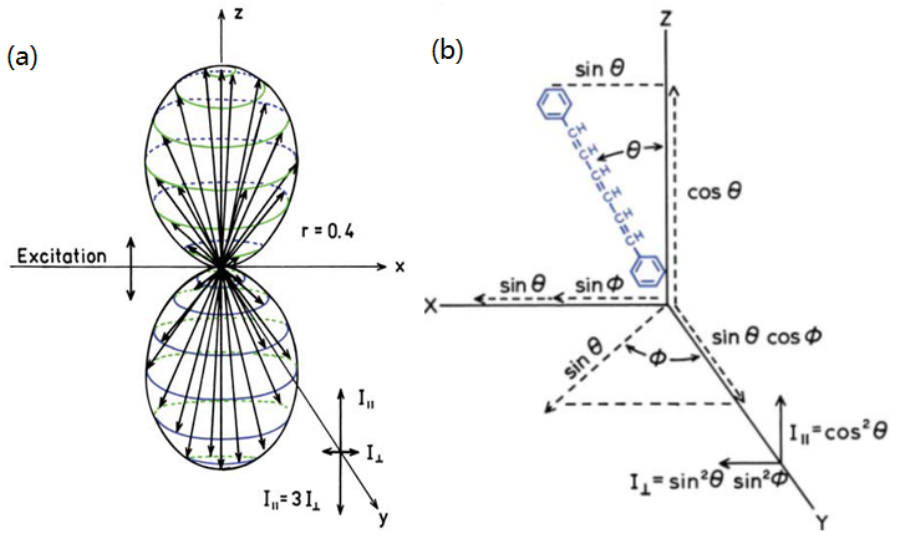

Figure 1.8 Excited-state distribution for immobile fluorophores with r0 = 0.4(a) and the emission intensities for a single fluorophore (b)[1]

From figure 1.8 (a), we can see that the light polarized intensity along an axis is proportional to projection of the transition moments into this axis, and as the excited-state population is symmetrical around the z-axis, the total intensity of $I_{\perp}$ would not be dependent upon φ. The parallel and perpendicular intensities for the molecule are given by

$$I_{\parallel} = \int_0^{\pi/2} f(\theta) I_{\parallel}(\theta) d\theta = \int_0^{\pi/2} f(\theta) \cos^2\theta d\theta \tag{1.10}$$

$$I_{\perp} = \int_0^{\pi/2} f(\theta) I_{\perp}(\theta) d\theta = \frac{1}{2}\int_0^{\pi/2} f(\theta) \sin^2\theta d\theta \tag{1.11}$$

And from the definition of anisotropy (Eq. 1.6), the anisotropy value can be calculated by:

$$r_0 = \frac{3\langle \cos^2\theta \rangle - 1}{2} \tag{1.12}$$

The term r_0 is used to refer to the anisotropy observed in the absence of other depolarizing processes such as rotational diffusion or energy transfer. A maximum anisotropy of 0.4 can be calculated from the equation above. This is the value that is observed when the absorption and emission dipoles are collinear, and when there are

no processes which result in depolarization. Under these conditions the excited-state population is preferentially oriented along the z-axis and the value of $I_{\parallel}$ is one-third the value of $I_{\perp}$.

Actually, for most fluorophores the r_0 values are less than 0.4, and in general the anisotropy values depend on the excitation wavelength. This is explained by the emission transition moments being displaced by an angle β relative to the absorption transitions. The observed anisotropy in a vitrified dilute solution is a product of the loss of anisotropy due to photoselection (2/5), and that due to the angular displacement of the dipoles. The fundamental anisotropy of a fluorophore is given by

$$r_0 = \frac{2}{5}\left(\frac{3\cos^2\beta - 1}{2}\right) \tag{1.13}$$

Where β is the angle between the absorption and emission transitions.

Suppose a fluorophore is excited with a pulse of vertically polarized light, and that it rotates with a single correlation time. The fluorescence intensity decay of the vertically ($I_{\parallel}$) and horizontally ($I_{\perp}$) polarized emission is determined separately. The decay of the difference between $I_{\parallel}(t)$ and $I_{\perp}(t)$, when properly normalized by the total intensity and corrected for the instrument response function, is the anisotropy decay (Figure 1.9).

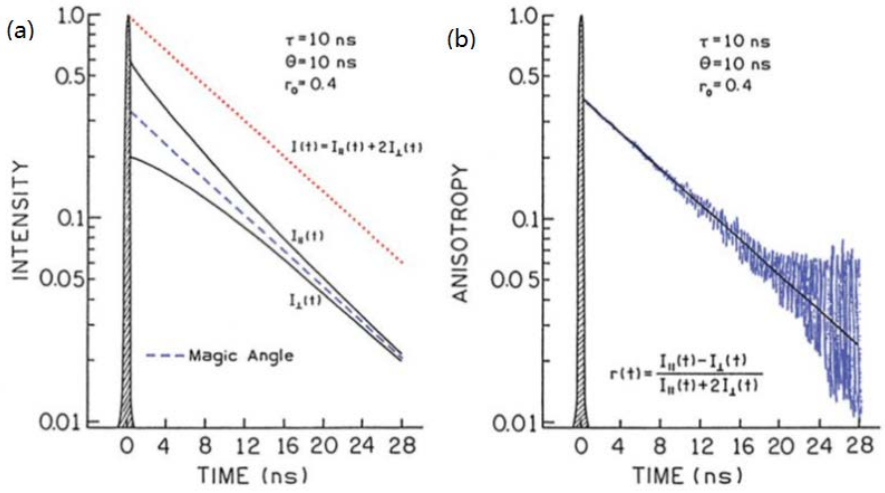

Figure 1.9 Time-dependent polarized decays (a) and the calculated anisotropy decay (b)[1]

In Figure 1.9 (a), the parallel component appears to decays more rapidly than the horizontal component at the beginning for the vertically oriented fluorophores are decaying through two processes at the same time: the intensity decay with decay time τ, and rotation out of the vertical orientation with correlation time θ, whereas the horizontal component initially decays more slowly for it is enriched by rotation from the excess vertically oriented emission.

The time-resolved fluorescence anisotropy decay of a sphere module could be described by the Perrin equation[2] as:

$$r(t) = r_0 e^{-t/\theta} = r_0 e^{-6Dt} \tag{1.14}$$

In this equation, θ is the rotational correlation time of the fluorophore, and D is the rotational diffusion coefficient. These two values could be calculated from the anisotropy decay curve.

If the flows in the solution are mainly laminar flow, the rotation of fluorophores would obey the Stokes-Einstein relationship from which we could get the relationship between the rotational diffusion coefficient and the viscosity of the solvent and the size of the rotating fluorophore:[3]

$$\zeta_r = 8\pi\eta R^3 \quad Stokes\ \ formula\ \ for\ rotation \tag{1.15}$$

$$\zeta_r D_r = k_B T \qquad Einstein\ relation \tag{1.16}$$

where η, k_B, R and T indicates the viscosity of the solution, Boltzmann constant, the radius of the particle and absolute temperature respectively, and ζ_r stands for the damping coefficient which is defined as the ratio of the applied force to the particle's terminal drift velocity.

From the Stokes-Einstein relationship and Perrin equation we obtain

$$\theta = \frac{1}{6D_r} = (\eta V)/(k_B T) \tag{1.17}$$

and from this the radius of rotating fluorophore could be calculate as:

$$R = \left(\frac{3\theta k_B T}{4\pi\eta} \right)^{\frac{1}{3}} \tag{1.18}$$

Thus the radius of the fluorophores could be calculated by measuring its fluorescence anisotropy decay.

1.2 Fluorescent Gold Nanoclusters

Noble metal nanoclusters typically consist of several to tens of atoms. Their scales are about one nanometer, and their properties are governed by their subnanometer dimensions. This size regime is comparable to the Fermi wavelength of the conduction electrons. The spatial confinement of free electrons in metal nanoclusters results in discrete and size-tunable electronic structures, leading to molecular-like properties such as luminescence and unique charging properties. Compared to semiconductor quantum dots (QDs), which are larger in dimensions (about 3 to 100 nm) and usually contain toxic metal species (e.g., cadmium, lead), noble metal nanoclusters are highly attractive for biosensing and bioimaging applications because of their ultrasmall size and nontoxicity.

1.2.1 Introduction to Fluorescent Gold Nanoclusters

Clusters, in general are aggregates of atoms that are large compared to atoms and molecules and small compared to small pieces of crystals. Unlike atoms and molecules as well as nanoparticles, clusters lay in a domain between these two which shows extraordinary different properties. Usually, clusters do not have the same structure or atomic arrangements as a bulk solid and can change their structures with the addition of just one or few atoms.

Gold nanoclusters (AuNCs) are attracting great attention in the field of nanotechnology. Because of their finite cluster sizes, these sub-nanometer clusters possess molecular-like electronic transitions between highest occupied molecular o orbital and lowest unoccupied molecular orbital (HOMO-LUMO) energy levels which can be rationalized according to the Jellium model ($E = \frac{E_{fermi}}{N^{\frac{1}{3}}}$).[4] Where E is the energy gap, E_{Fermi} is the Fermi energy and N is the number of atoms. AuNCs

demonstrate unique fluorescent optical properties due to its electronic nature, and provide new opportunities for optical applications.

Synthesis of gold nanoclusters, unlike that for gold nanoparticles which is a well-explored field in nanotechnology[5], is a relatively new and developing field. The isolation and purification of AuNCs has been a recent scientific achievement, leading to many thorough investigations of both their structure and implications for nanotechnology.[6]

Among all the efforts to characterize AuNCs, Mass spectrometry and x-ray spectroscopy proved to be most successful. Mass spectrometry alone can provide reliable information about the size of the gold core and capping ligand environment.[7,8] Obtaining these parameters can lead to a quantitative analysis of Au NCs composition.

X-ray spectroscopy techniques offer a site-specific determination of local structure for Au NCs which are on the topic of probing the structure of protein protected Au NCs. One of the techniques which is extensively used in Au NC and NP research is x-ray photoelectron spectroscopy (XPS) which provide information on the oxidation state of gold clusters by examining the $4f_{7/2}$and $4f_{5/2}$ binding energies of protein-stabilized Au NCs. [9,10,11]

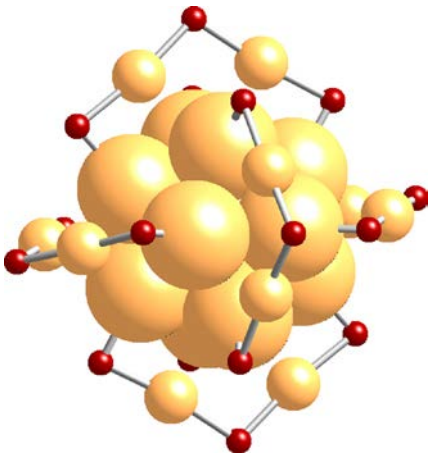

Figure 1.10 A model of the Au25NC with surface staple motif "S-Au-S-Au-S". Organic capping ligands are omitted for clarity of the Au25NC structure[12]

Computational and theoretical studies have also played a big part in probing the electronic structure. Some of the unique electronic effects of AuNCs can be attributed

to a surface staple-like bonding structure between the organic capping ligand and surface gold atoms (Fig. 1.10).

1.2.2 Synthetic Methods of Fluorescent Gold Nanoclusters

Synthetic methods of fluorescent gold nanoclusters have developed rather rapidly in the decade, and an "atom to cluster" synthesis route has been developed using various biological organisms.[13]

Biological organisms can intake metal atoms to form mineral structures subsequently, and this natural process is called biomineralization. As a consequence, nanostructures can be formed when biological organism or macromolecule naturally intake and arrange inorganic materials.[14]

Proteins, as biological macromolecules, have certain configuration and spaces and can be utilized as templates for preparing fluorescent AuNCs. Synthesis method using proteins as templates generates highly stable gold nanoparticles and protein-encapsulated gold nanoclusters have attracted intense investigation recently.[15]

Based on this biomineralization, incorporating proteins with gold atom precursors have evolved into a novel one-step synthesis, producing stable and fluorescent AuNCs.

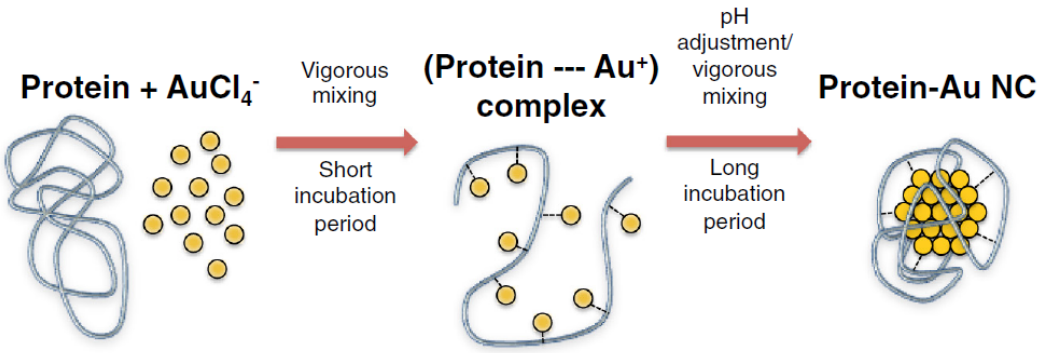

Figure 1.11 Typical reaction pathway for an AuNCs synthesis[12]

There are many advantages to this one-step synthetic approach, such as relatively low environmental impact: mild reaction conditions, aqueous solution reaction environment, and absence of strong reducing agents make the growth of AuNCs a

green chemical synthesis. Generally, pH conditions are of great significance in the reaction for they can optimize the protein's reducing ability and increase organic-metal bonding and stabilization. Figure 1.11 shows a typical reaction pathway for a AuNCs synthesis.

The formation of a single gold nanocluster product is highly dependent on the conformation of the protein for it plays a vital role of stabilizing, reducing, and arranging gold atoms into stable nanoclusters.[16] One of the most significant advantanges of these water-soluble AuNCs is how readily they can be used in applications because of their immediate biocompatibility. Already, many proteins have been used as stabilizing agents and reducing agents for AuNCs such as BSA,[17] lysozyme,[18] human transferrin,[9] lactoferrin,[19] pepsin,[20] and horseradish peroxidase.[21]

Proteins serve as both stabilizing and reduction agents in the synthesis of AuNCs because certain kinds of amino acids have strong reducing strength and favorable binding interactions with gold. However, the synthesis of metal nanoclusters is a relatively slow process (usually taking days) and only certain sequences of amino acids can promote nanocluster growth while others will have little interaction with metal ions. It is still difficult to establish relationships between amino acid sequence and reaction efficiency as proteins usually have various compositions and structures. A "bottom-up" approach was used by Tan et al. to formulate a set of primary rules for the size- and shape-controlled peptide synthesis of gold nanoclusters from the 20 natural amino acid residues for $AuCl_4^-$ reduction and binding to Au^0.[22] The results show that the presence of certain reducing amino acid residues whose activity may be regulated by neighboring residues with different Au^0 binding strengths is vital to the reduction capability of a peptide.

To understand the growth mechanism of gold nanoclusters, Luo et al. revealed the detailed process from reduction of Au(I)−thiolate complex precursors to the eventual evolution of and focusing to the atomically precise Au_{25} NCs by monitoring the time evolution of Au(I) precursor and Au NC intermediate species with ESI-MS.[23] A two-stage formation and growth process was proposed: a fast stage of reduction-growth mechanism where Au (III) was reduced to Au(i) and Au(0), followed by a slow stage

of intercluster conversion and focusing which finalize the synthesis with stable Au_{25} nanoclusters.

1.2.3 Optical Properties of Fluorescent Gold Nanoclusters

As the size of noble metal nanoclusters are comparable to the Fermi wavelength of electrons which is about 0.5 nm for gold, they are too small to have the continuous density of states necessary to support a surface plasmon. However, noble metal nanoclusters exhibit very unique fluorescent characteristics dependent on nanocluster size, geometry and chemical states. Though significant advances had been achieved in their synthesis methods and some applications have been demonstrated, the origin of the fluorescence and their fluorescent mechanism still remain unclear.

The discovery of AuNCs fluorescence was reported in 1998, stating that fluorescence intensity will increase with decreasing nanoparticle size.[24] This transition can be seen when surface plasmon resonance from gold nanoparticles vanishes and fluorescence appears as the size of the particle decreases.

Essentially, the emission wavelength is determined by the number of atoms following the Jellium model:[4]

$$\hbar\omega_0 = 3.61 \bullet \frac{\hbar^2}{2\mu r_s^2}(N)^{-\frac{1}{3}} \tag{1.19}$$

which indicates that the energy of emission light is proportional to $N^{-\frac{1}{3}}$. However, slightly different fluorescence was observed in Au_{25} NCs with various ligands from the red to near-infrared.[25,26] Furthermore, even with the same BSA ligand, fluorescence of the nanoclusters would be influenced by the PH of the solution.[27] These studies confirmed that the red fluorescence is determined not only by the cluster itself but also by the ligands and surrounding environment.

The atomic structure of AuNCs has been extensively studied. [28] It is believed that Au_{25} NCs have a core−shell structure in which 13 Au(0) atoms form an icosahedral core surrounded by 6 $Au_2(SR)_3$ staples.[6,29] Such a structure suggested that surface ligands play a vital role in the electron structure of the clusters as well as their optical properties.[29]

AuNCs exhibit molecule-like electronic structure with an energy gap, from the highest occupied molecular orbital (HOMO) to lowest unoccupied molecular orbital (LUMO). As a result, the interband radiative transition lifetime is usually very short for AuNCs, ranging from picoseconds to nanoseconds. However, for some nanoclusters long microsecond component decay has been observed, as well as a short nanosecond component. Two luminescence emissions at 1.5 and 1.15 eV in glutathione-protected Au_{28} NCs has been observed and assigned to fluorescence and phosphorescence, respectively.[30] Controversially, other researchers suggested that the luminescence originates from interband transition of the clusters, and charge transfer from the surface ligands to the core plays a major role in the red fluorescence.[29]

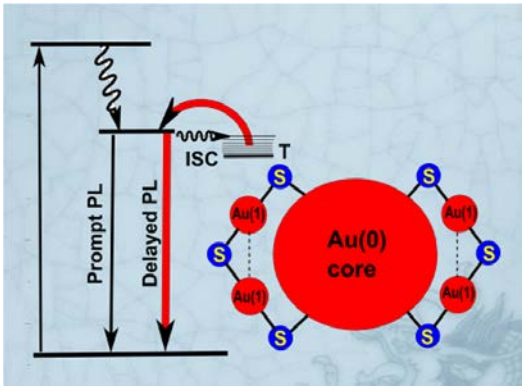

Figure 1.12 Fluorescence mechanism and diagrammatic sketch of AuNCs[27]

Studies which specifically focus on the time resolved fluorescence and transient absorption of Au_{25} NCs in the time scales of picoseconds to microseconds have been made to obtain detailed insight for physical understanding of the fluorescent mechanism of nanoclusters,[27] and the results indicate that the fluorescence of BSA-protected Au_{25} NCs consists of prompt fluorescence (PF) in a nanosecond time scale and delayed fluorescence (DF) in a microsecond time scale (Fig. 1.12). The observed long decay component regarded as delayed fluorescence is a consequence of efficient intersystem crossings (ISC) and later reversed intersystem crossings (RISC) between the singlet and the triplet states due to a very small energy gap between these two states. The study also suggests that the conjugation of BSA can influence the electronic structure of Au_{25} NCs and the dynamics in the fluorescence. The triplet states are quite relevant to the Au (I)-S semiring and Au (I) complex.

1.2.4 Applications of Fluorescent Gold Nanoclusters in Life Science

Fluorescent probes play an important role in the development of fluorescence-based imaging techniques for life sciences research. Fluorescent AuNCs have an attractive set of features including ultrasmall size, good biocompatibility and photostability, and tunable emission in the red to near-infrared spectral region, which make them promising as fluorescent labels for biosensing and bioimaging.

The detection of toxic metals (Hg^{2+}, Cd^{2+}, Pb^{2+}) in solution is one of the applications for Au NPs in biosensing.[31] The interactions between heavy metal ions and Au NPs can be detected by changes in the UV-Vis absorption due to the aggregation or chelation of Au NPs.[32]

In a similar manner, protein protected Au NCs were also studied for their applications in metal ion sensing. It was discovered that BSA protected Au NCs have a selective interaction with Hg^{2+},[33,34,35] which quenches the fluorescence linearly with increasing Hg^{2+} concentration. Several proposed mechanisms for fluorescence quenching were discussed in the literature. One proposed that the highly metallophilic bonding between Hg^{2+} and Au^{+} disrupts the fluorescence from Au-BSA interactions.[33] Yet another suggested that the quenching is a consequence of a photo-induced electron transfer process when Hg-S bonds are formed from BSA, intercepting one of the charge carriers during the excitation process and reducing Hg^{2+} to Hg^{+}.[36] The other possible quenching mechanism is a process called cyanide etching which removes gold atoms from the gold core.[37] Detection limits for sensing Hg^{2+} have been very low, ranging from 80 nM[36] to 0.5 nM.[33]

Although not as notable as Hg^{2+}, Cu^{2+} has a quenching effect on BSA protected Au NCs as well, and the mechanism of the quenching is believed to Cu^{2+} ions binding to BSA rather than the fluorescence quenching by metal–metal interaction as in the case of Hg^{2+}.[38,39,38,40] With a detection limit around 50 mM, Au NCs was proved to be an efficient probe for Cu^{2+} in absence of Hg^{2+}.

In the field of bioimaging, Au NCs were used as an imaging probe for detection of foliate receptors by conjugate folic acid to the surface of BSA through amine

linkages[41,42]. Results show that Au NCs could provide a feasible and low toxic method for selectively detecting and imaging cancer cells for only a minor reduction in the quantum yield was detected after the bioconjugation of folic acid. And by bioconjugation with other receptor-targeting biomolecules, Au NCs could be used for targeted imaging applications in more ways than one.

Insulin protected Au NCs showed great biocompatibility and cell internalization for fluorescence based cell imaging. Fig. 1.13 shows internalization of fluorescent insulin-Au NCs inside myoblast cells, demonstrating Au NCs as a promising imaging probe.[43]

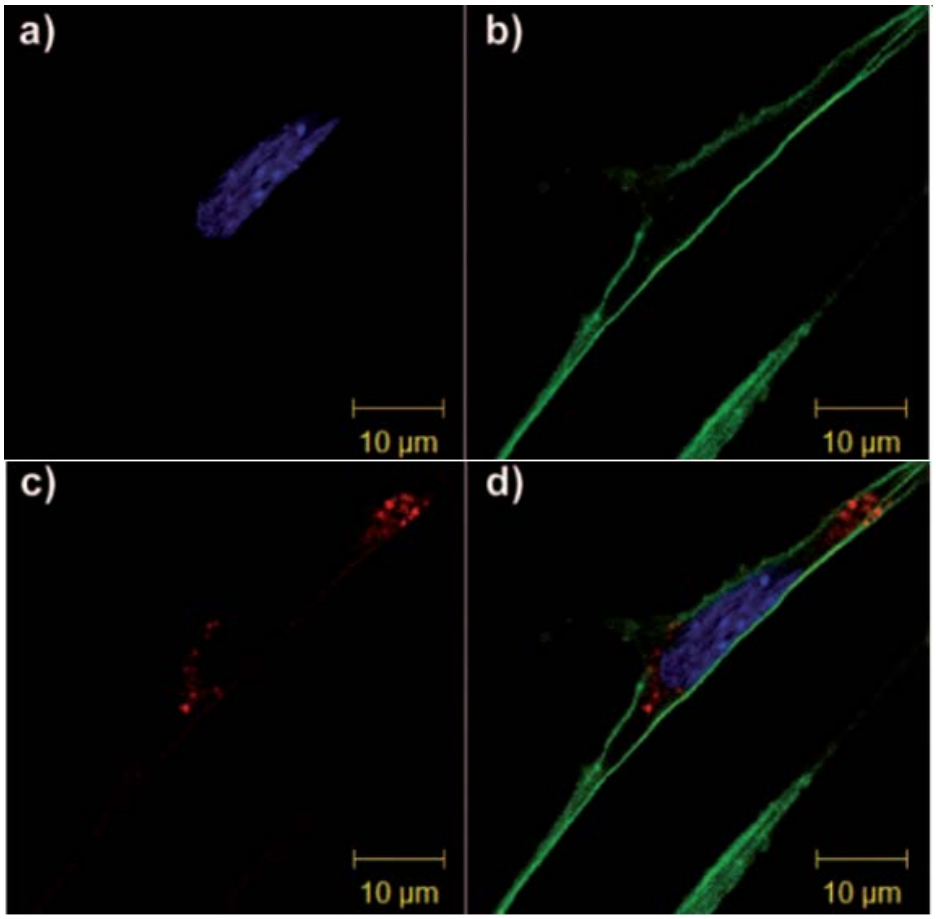

Figure 1.13 Internalization of fluorescent insulin-Au NCs inside myoblast cells. The as-prepared Au NCs retain their strong red fluorescence inside the cell. Fluorescent staining of the cell nucleus (blue) and cell wall (green) is also shown[20].

2. Experimental

Along with the exploration of photonics, a wide verity of spectroscopic techniques have been developed to providing complementary and unique information, among which fluorescence continues to facilitate many important observations and techniques across a whole range of disciplines. Fluorescence has made, and continues to make, particular impact in the biosciences and in healthcare. This has been dramatically demonstrated in recent years by the key role played by fluorescence in the complete sequencing of the human genome and in the displacement of radioactive markers by fluorescence probes in disease diagnostics.

When the readily accessible properties of fluorescence are combined with the high sensitivity afforded by photon counting photonics, fluorescence has enabled the ultimate limit of single molecule detection to be realized and this in turn is helping to open up new frontiers, such as molecular pathology, whereby metabolism, disease and pharmacology can be studied at the most fundamental level.

2.1 Absorption and Fluorescence Spectroscopy

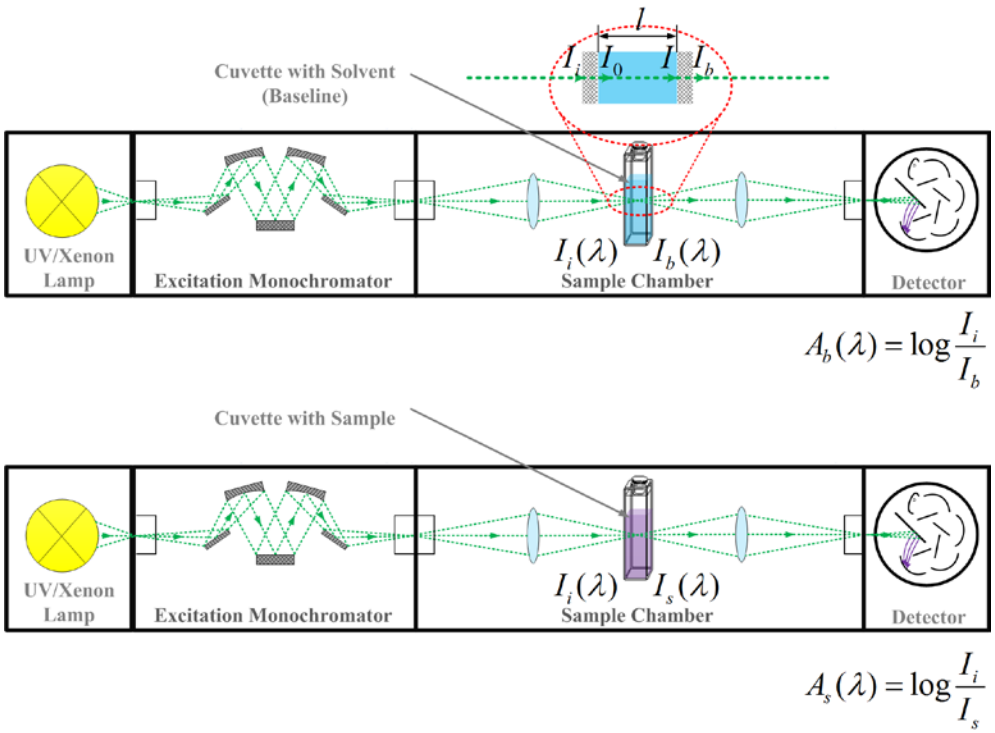

Figure 2.1 Typical spectrophotometer schematic for recording excitation spectra

Absorption spectroscopy refers to spectroscopic techniques that measure the absorption of radiation due to its interaction with particle solutions. The intensity of the absorption varies with different emission wavelength, and the collection of intensity of a certain solution with a given range of wavelength or frequency is the absorption spectrum. Figure 2.1 shows a typical Spectrophotometer schematic and usually how absorption spectra are measured.

As in figure 2.1, a spectrophotometer usually comprises a light source containing a UV lamp and a Xenon Lamp, an excitation monochromator which is used to tune the incident light into a narrow band of wavelength, a sample chamber and a detector.

According to the Beer-Lambert Law, the transmittance of light through a substance is dependent logarithmically on the attenuation coefficient of the substance, and the distance the light travels through the material respectively. As in the case of solution:

$$I(\lambda) = I_i(\lambda)10^{-\varepsilon(\lambda)cl} \tag{2.1}$$

Where $I(\lambda)$ is the transmitted intensity after absorption, $I_i(\lambda)$ is the incident intensity, c is the molar concentration of the solution, l is the light path length (as the l in figure 2.1), and $\varepsilon(\lambda)$ is the decadic molar extinction coefficient. $\varepsilon(\lambda)cl$ is defined as the optical density indicating the absorption ability of the sample.

As shown in figure 2.1, the measurement of absorption spectra of a sample solution usually takes two steps: first, the transmitted intensity through the solvent of the solution such as distilled water $I_b(\lambda)$ was measured to create a base line; then the solution sample's transmitted intensity $I_s(\lambda)$ was measured. According to Beer-Lambert Law, the optical densities of a mixture with different components has a linear relationship when their values are very low (much smaller than 1). So the optical density of the sample would be

$$\varepsilon(\lambda)cl \approx A(\lambda) = A_s(\lambda) - A_b(\lambda) = \log\frac{I_s(\lambda)}{I_i(\lambda)} - \log\frac{I_b(\lambda)}{I_i(\lambda)} = \log\frac{I_s(\lambda)}{I_b(\lambda)} \tag{2.2}$$

Where the ordinate of the absorption spectrum $\varepsilon(\lambda)$ could be obtained.

Fluorescence spectroscopy refers to the spectroscopic techniques which acquire and analyze fluorescence from a fluorescent sample. The devices used to measure fluorescence are called fluorimeters whose configurations are shown in figure 2.2.

As shown in figure 2.2, a fluorimeter mainly consist of a xenon light source, excitation monochromator, sample chamber, emission monochromator and photomultiplier detector. Additional optical components such as focusing mirrors and lenses, light filters which are used to stop the scattering light from the sample and polarizers which are mostly used in anisotropy measurement would be applied when necessary.

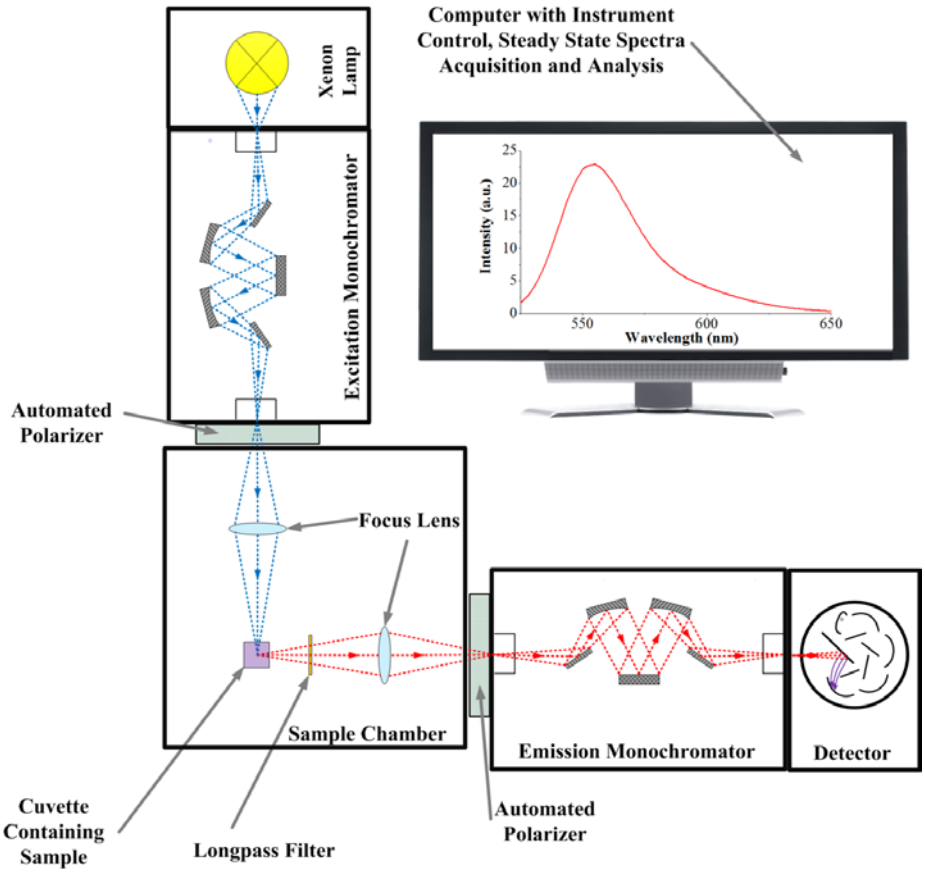

Figure 2.2 Typical fluorimeter schematic for recording fluorescence spectra

After placing the to-be-measured sample in the sample chamber, the measurement parameters could be set through a connected computer and the fluorescence spectra could be acquired automatically. However, a correction factor which is unique each machine has to be applied to the measured fluorescence spectra due to the differing detection efficiency per wavelength of the fluorimeter. The wavelength correction

factor is the ratio of the measured fluorescence intensity to the actual fluorescence intensity.

2.2 Lifetime and Anisotropy Measurement

Pulse fluorometry in the time domain and phase-modulation fluorometry in the frequency domain are the two main approaches to measuring fluorescence lifetime. As linked by Fourier transforms, these two different approaches are, equivalent and complementary theoretically. However, some significant differences emerged in experimental implementation and data-analysis: in phase-modulation, the fluorescence lifetime is determined from either the phase shift or modulation depth of fluorescence with respect to excitation while the excitation light is modulated or chopped; in pulse fluorometry the fluorescence lifetime are acquired in forms more resemble to an exponential decay with a temporally sharp excitation.

Although phase-modulation fluorometry possess a higher measuring speed under certain circumstances, pulse fluorometry has found more widespread favour for fluorescence lifetime measurement for its simplicity and adaptability. The most popular technique of pulse fluorometry is time-correlated single-photon counting (TCSPC) which based on delayed coincidence techniques developed for nuclear physics and then adapted for recording scintillation decay.

Generally, TCSPC is a process that the times of individual photons detection by a photo-multiplier after a single pulse would be recorded repeatedly until enough recorded events are gained that they could be used to build a decay curve of the number of events across all of these recorded time points. This decay curve can then be fit to an exponential function or functions that contain the exponential lifetime decay function. [44]

TCSPC and its variants have some notable advantages over other methods, particularly when researching unknown kinetics:

1. Easily enhanced data precision through increasing measurement time
2. Intelligible time-correlated decay curve
3. Easy data analysis with known statistical basis (Poisson)
4. Minimize signal amplitude variations

Figure 2.3 shows the schematic of a typical TCSPC fluorometer. This setup shares many similarities to the fluorimeter shown in Figure 2.2, showing how hybrid instruments can be easily engineered by changing components or routing light paths. Sometimes a semiconductor laser diode (LD) or light emitting diode (LED) which could provide monochromatic light pulse with ultra-high frequency would be used as light source instead of a lamp and excitation monochromator. Polarizers are used mainly for anisotropy measurement. Generally not needed for lifetime measurements with low viscosity solvents such as water, ethanol and cyclohexane, polarizers should be applied when the fluorophore rotational correlation time is comparable to fluorescent lifetime in order to correct for any intrinsic polarization of the fluorimeter.

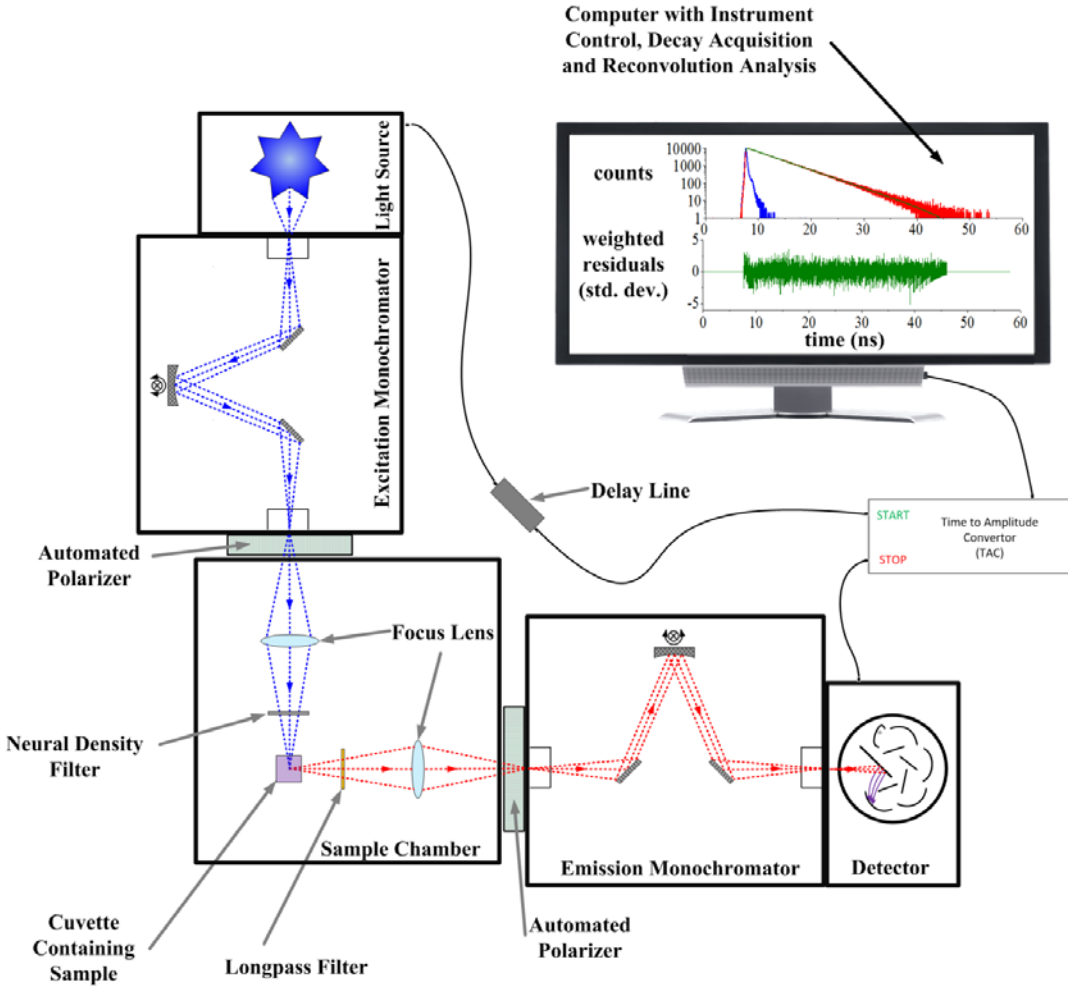

Figure 2.3 Schematic of a typical pulse fluorometer

There are several ways to measure the “start”-“stop” time interval between excitation of fluorescence and its detection, among which include fast oscilloscopes, sampling

oscilloscopes (boxcar integrators), multichannel scaling, stroboscopic detector gating and time to amplitude convertor (TAC), as traditionally used in TCSPC, whereas ,in this way, the time interval between excitations were also known as the tac range. The TAC converts the time difference to a voltage v, which is then digitized in an analogue to digital convertor and stored as a detected photon count event in a multi-channel analyzer (MCA). Repeating the cycle in accordance with the excitation pulse frequency allows a histogram of counts to be accumulated to build a decay curve with the recorded counts at time t as the ordinates of time t.

The method of least squares is usually used to fit the fluorescence lifetime decay where a quantity χ^2 is used as a measure of mismatch between data and fitted function, and by definition

$$\chi^2 = \sum_{DATA} [\frac{Y(i) - F_y(i)}{\sigma(i)}]^2 = \sum_{DATA} [\frac{\text{actual deviation}}{\text{expected deviation}}]^2 \qquad (2.3)$$

Where $Y(i)$ is the fluorescence decay datum value, $F_y(i)$ is the fitting function value and $\sigma(i)$ is the statistical uncertainty of the datum value $Y(i)$ (standard deviation). If the fitting function is appropriate, then the minimum χ^2 should be characterized by equaility between actual and expected deviations. Thus for a good fit the normalized χ^2(CHISQ) should be

$$\chi_N^2 = \frac{\chi^2}{N - v} \approx 1 \qquad (2.4)$$

where N is the number of data points and v is number of fitted parameters and the quantity ($N - v$) is referred to as the number of the degree of freedom.

The compliment used to measure anisotropy decay should be the same as lifetime measurement (figure 2.3), with the excitation and emission polarizer. And in this case the time-resolved anisotropy function should be:

$$r(t) = \frac{I_{VV}(t) - GI_{VH}(t)}{I_{VV}(t) + 2GI_{VH}(t)} \qquad (2.5)$$

Where I_{VV} the observed intensity when both excitation and emission polarizers are vertical, I_{VH} represents the observed intensity when the excitation polarizer is horizontal while the emission polarizer is vertical, and G ($G = I_{HV} / I_{HH}$) is a factor determined for horizontal orientation of the excitation polarizer in order to correct for differences in the polarization transmissions of the fluorescence detection channel, which are largely due to the emission monochromator.

In order to ensure any fluctuations in the source intensity are corrected, the measurement of I_{VV} and I_{VH} would be conducted in turn to average out any drift, and sometimes a T-format would be used to offer continuous correction.

From equation 2.5, construct two new decay curves:

$$S(t) = I_{VV}(t) - GI_{VH}(t) \tag{2.6}$$

$$D(t) = I_{VV}(t) + 2GI_{VH}(t) \tag{2.7}$$

Which could be analysed separately, and when they are combined, the anisotropy decay curve could be obtained. Finally

$$\chi^2 = \sum_{DataPts} [\frac{D(t) - S(t) \otimes r(t)}{\sqrt{D(t)}}]^2 \tag{2.8}$$

could be used to evaluate the quality of the fitting.

2.3 Fluorescence microscopy

A fluorescence microscope is an optical microscope that uses fluorescence instead of, or in addition to, reflection and absorption to study properties of organic or inorganic substances.[45] Fluorescence microscopy is a non-invasive, non-destructive technique, capable of imaging at levels from a single molecule, cell, tissue, to a whole individual. With its spatial resolution, sensitivity, selectivity and dynamical insight, fluorescence microscopy has become a prominent technique in biological research for its capability

to visualize biomolecules which enables the study of elementary biochemical reactions in living cells.

The term "fluorescence microscope" refers to any microscope that uses fluorescence to generate an image, whether it is a simple conventional one like a wide-field fluorescence microscope, which traditionally operated with only incoherent optical excitation, such as from a high pressure mercury lamp fitted with a wavelength filter, or a more complicated design such as a confocal microscope, which increases optical resolution and contrast by adding a spatial pinhole placed at the confocal plane of the lens to eliminate out-of-focus light.[46]

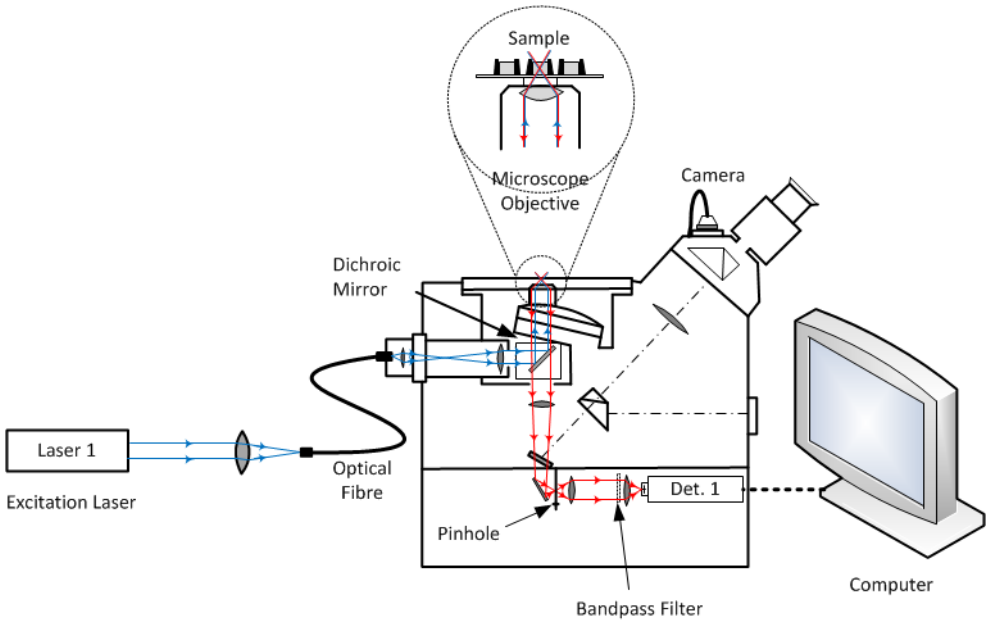

2.4 Schematics of a confocal microscope

The subsequent development of the confocal microscope and laser-based techniques greatly improved the spatial resolution and imaging capability of fluorescence microscopes. In a confocal microscope, as shown in Figure 2.4 samples are illuminated through a pinhole aperture and the fluorescence signal is channelled via another pinhole near the detector. The image is then compiled from laser scans of the surface. In this way, the microscope is able to discriminate against “out-of-focus” signals. Thus confocal microscopes overcome some of the resolution difficulties associated with wide-field optical microscopes and allow the reconstruction of three dimensional structures from the images obtained.

3. Optical Properties of BSA-AuNCs

The optical properties are the most important features of a fluorephore as they not only determine the usage of the fluorephore in biosensing or bioimaging, but also manifest its structure and fluorescence mechanism.

In this chapter, steady-state and dynamic spectroscopic studies of bovine serum albumin (BSA) protected Au nanoclusters synthesized at different PH are presented and the influence of pH on the fluorescence properties is discussed. The steady-state study focuses on the dependence of fluorescent wavelength on pH which has rarely been reported; the lifetime study extends the study of the relation between the emission wavelenth and synthesis pH by separating the long decay and short decay components of the lifetime decay curve. A mass spectroscopic study is also reported here which intend to provide a possible explanation for the origins of the two fluorescent peaks and multiple decay components.

3.1 Sample Preparation

The nanoclusters used in this thesis are red emission BSA-AuNCs consisting of 25 gold atoms which are synthesised through a simple, one-pot, “green” synthetic route. This synthesis method based on the capability of a common commercially available protein, bovine serum albumin, which is used as both protecting protein and reduction agent.

Figure 3.1 illustrates a schematic of the formation of Au NCs in BSA solution[17]: in a typical synthesis, HAuCl4 solution (5 mL,10 mM, 37 °C) was added to BSA solution (5 mL, 50 mg/mL,37 °C) under vigorous stirring. Two minutes later, NaOH solution (0.3-0.8 mL, 1 M) was introduced, and the mixture was incubated at 37 °C for about 2-12 hours which is dependent on the synthesis pH with continuous stirring. Then the mixture would be kept in a 37 °C thermostat for several days. The nanoclusters are stable under room temperature or daylight.

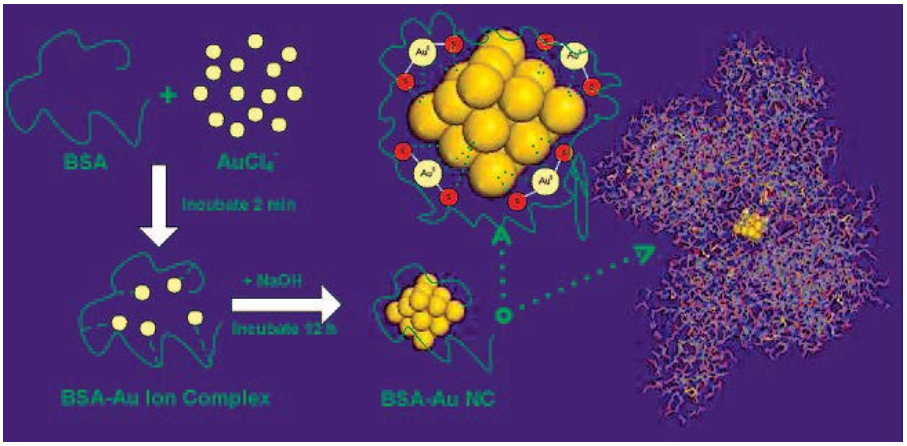

Figure 3.1 Schematic of the formation of Au NCs in BSA solution[17]

The synthesis of fluorescent BSA-AuNCs is sensitive to pH: fluorescent nanoclusters can only be formed under a narrow range of pH which is high enough to activate the reduction ability of BSA while low enough so that the BSA would not be deformed. The pH during synthesis was measured by a pH electrode in a control sample so that the sample for further study would not be contaminated. The relationship between the pH and the volume of added NaOH solution (1M) is shown in Fig. 3.2

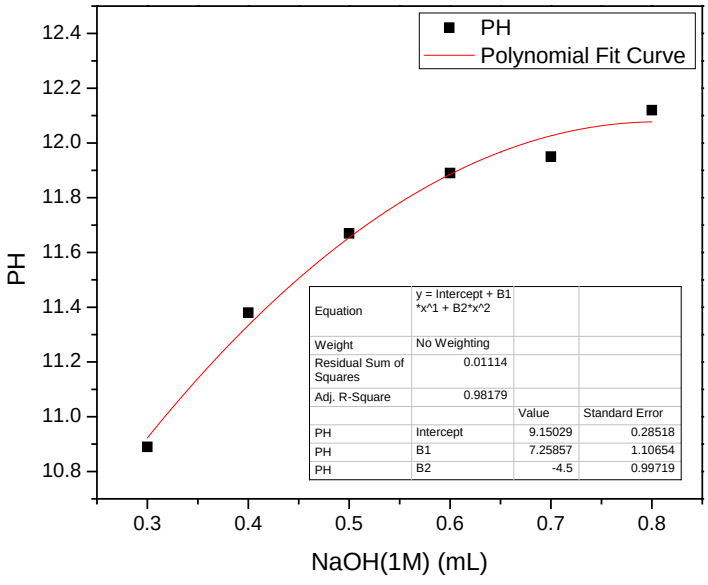

Figure 3.2 Relationship between pH and added NaOH solution

BSA-AuNCs samples with various pH from 11.38 to 12.12 were made by changing the amount of NaOH used in growth. The colour of the solution changed from light yellow to light brown, and then to various colours from red brown to dark brown under normal daylight with different pH (Fig. 3.3).

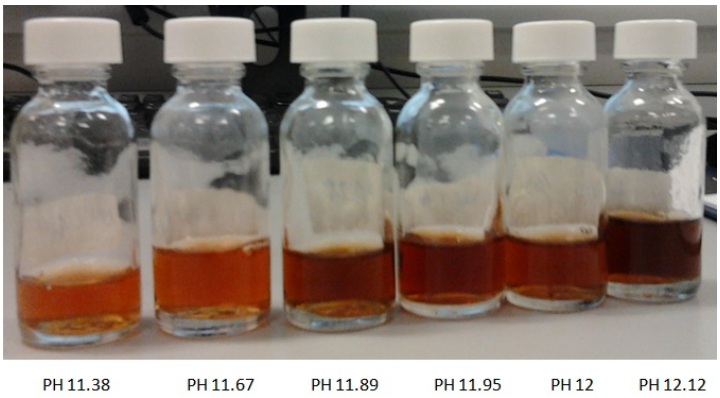

Figure 3.3 AuNCs aamples of different pH

3.2 Fluorescence spectra of AuNCs synthesized at different pH

Figure 3.4 shows the emission spectra of the sample under pH 11.67 (ten times diluted) with various excitations from 400nm to 500nm. There are no apparent changes in peak position as excitation was varied. However the rising edge and falling edge are not symmetric suggesting that there might be multiple fluorescent emission peaks. These emission peaks from the BSA-AuNCs might arise from different excited states involved in luminescence processes or different luminescence mechanism of same BSA-AuNCs, or luminescence of BSA-AuNCs of different gold core sizes/structures.

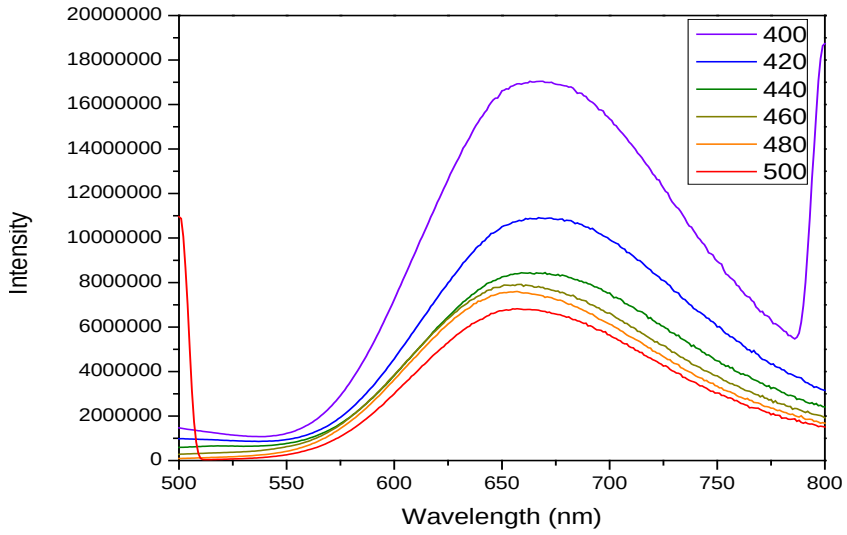

Figure 3.4 Emission spectrum of AuNCs with various excitation wavelengths

Figure 3.4 also shows that shorter excitation wavelength (400nm) generates stronger fluorescent intensity. However as the excitation wavelength become shorter, the fluorescence from BSA around 500nm also becomes stronger. To minimize its interference on the study of AuNCs' optical properties, excitation wavelength of 480nm was used in further studies on the emission properties of BSA-AuNCs in this thesis.

Table 3.1 Culmination wavelength with different pH

PH	11.38	11.67	11.89	11.95	12.00	12.12
Culmination (nm)	656	650	689	680	690	710

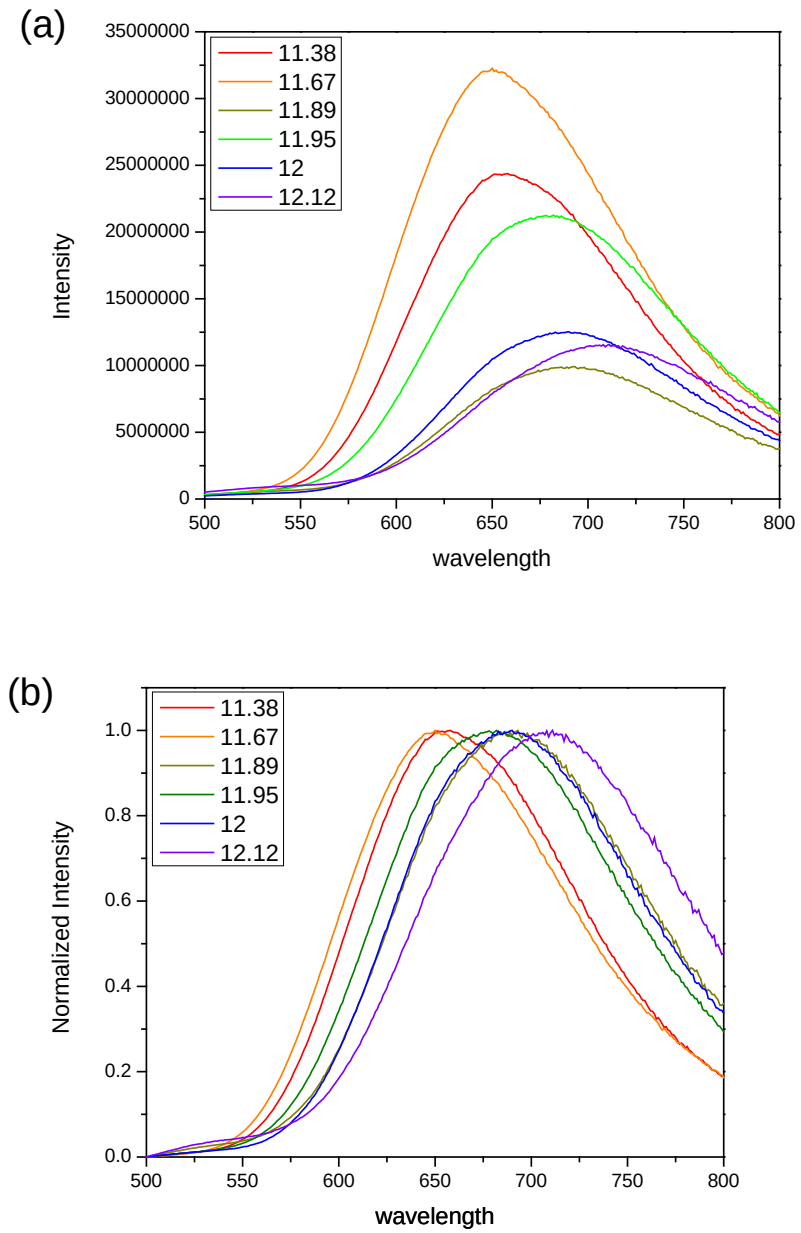

Figure 3.5 Emission spectra(a) and normalized emission spectrum(b) of AuNCs with different pH with excitation wavelength of 480nm

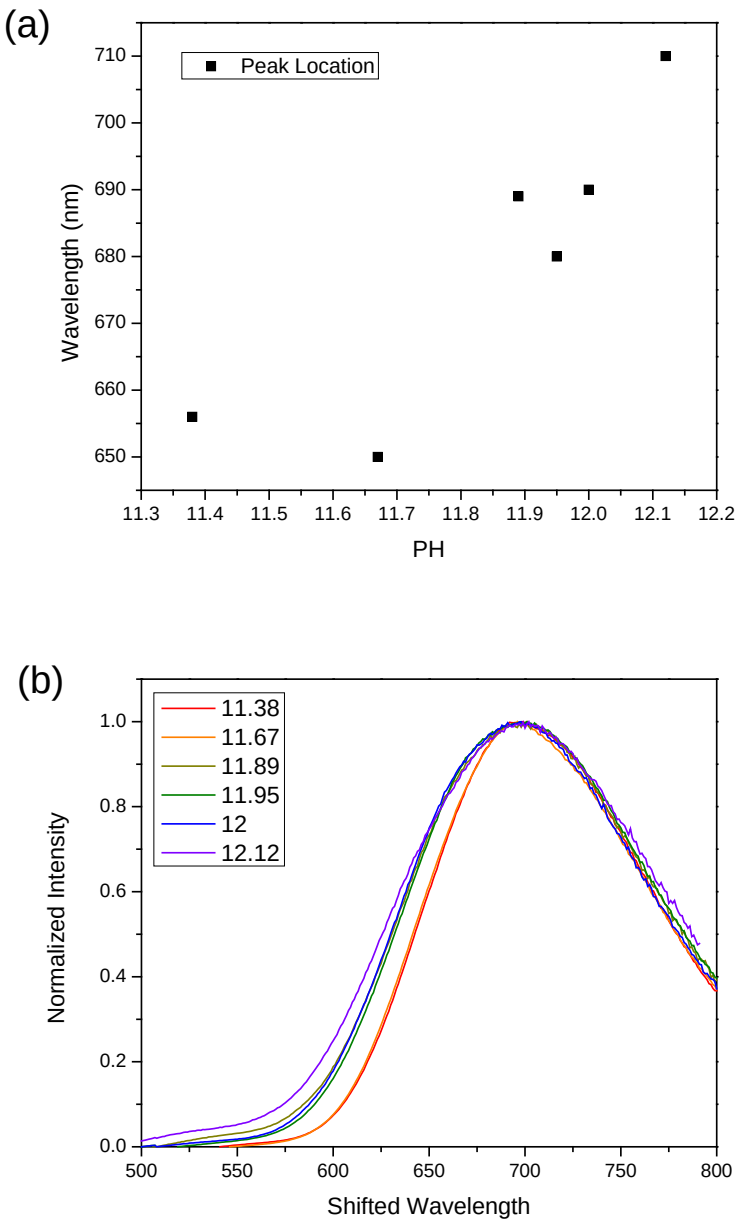

Figure 3.6 (a) The relationship between emission spectra peak position and synthesis pH; (b) normalized emission spectra of AuNCs with different pH with their peaks moved to 690nm

The emission spectra of AuNCs with different pH, figure 3.5(a), show that the fluorescence intensity changes with pH and the sample with pH of 11.67 has the highest emission intensity under the excitation of 480nm. In addition, the position of the emission peaks are quite different as the synthesis pH changes as shown in figure 3.5(b) where emission spectra are normalized; the culmination position of each spectra are listed in table 3.1. Figure 3.6 (a) shows the trend of culmination position change: significant spectra shift to longer wavelength could be observed as synthesis pH rises.

Furthermore, the shape of the emission was also compared, as shown in figure 3.5 (b) where emission spectra of different pH were moved to align the peaks at 690nm; several facts could be concluded from this figure:

1. The shape of each spectrum is different.

2. There's a trend as the higher the synthesis pH (the longer the peak position wavelength), the wider the peak would be.

3. The shapes of the falling edge of each spectrum, though their spectral positions are different, are very similar; however the shapes of the rising edge change significantly as the pH changes.

The emission spectra were fitted with multiple Gaussian peaks using Origin. Fig. 3.7 shows the fitted spectra under pH of 11.67 and 12.12; both spectra could be nicely fitted with four Gaussian peaks and the ratio of intensity between the three main peaks changes remarkably with different pH. The Detailed fitting results are included in table 3.2.

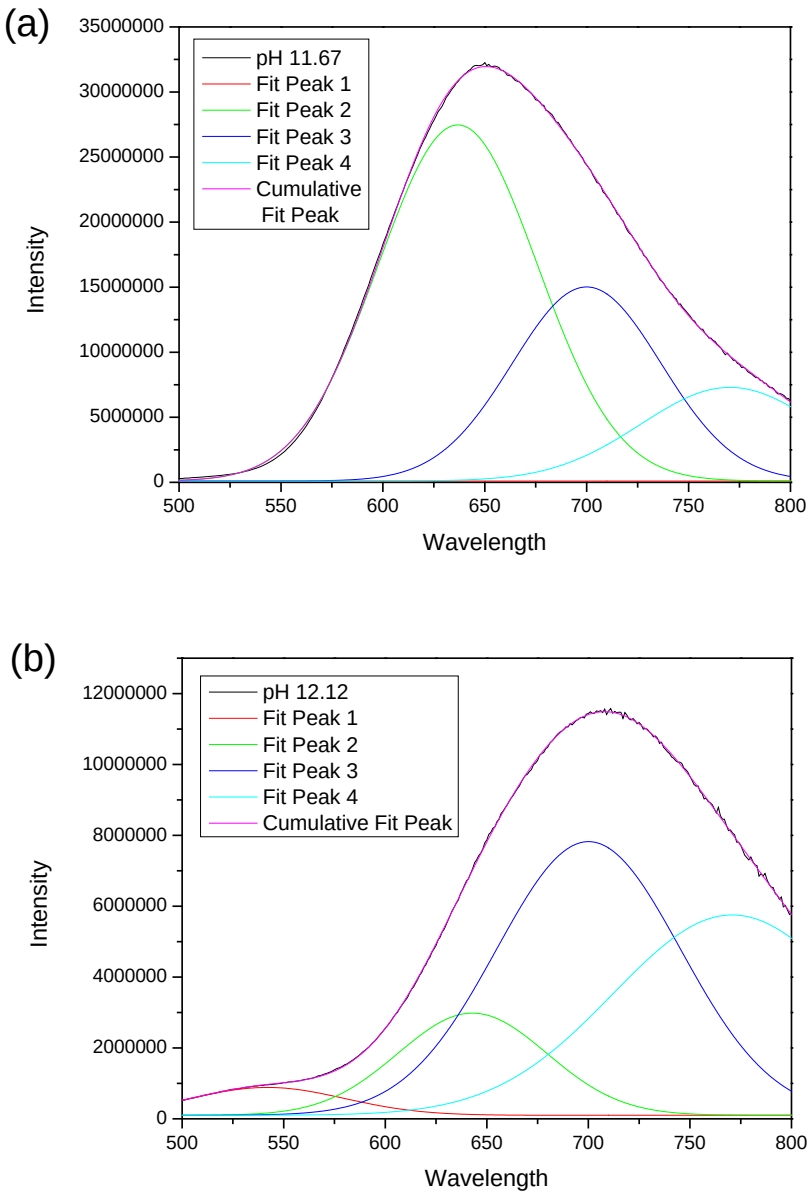

Figure 3.7 Two fitted emission spectra of BSA-AuNCs under pH 11.67(a) and 12.12(b)

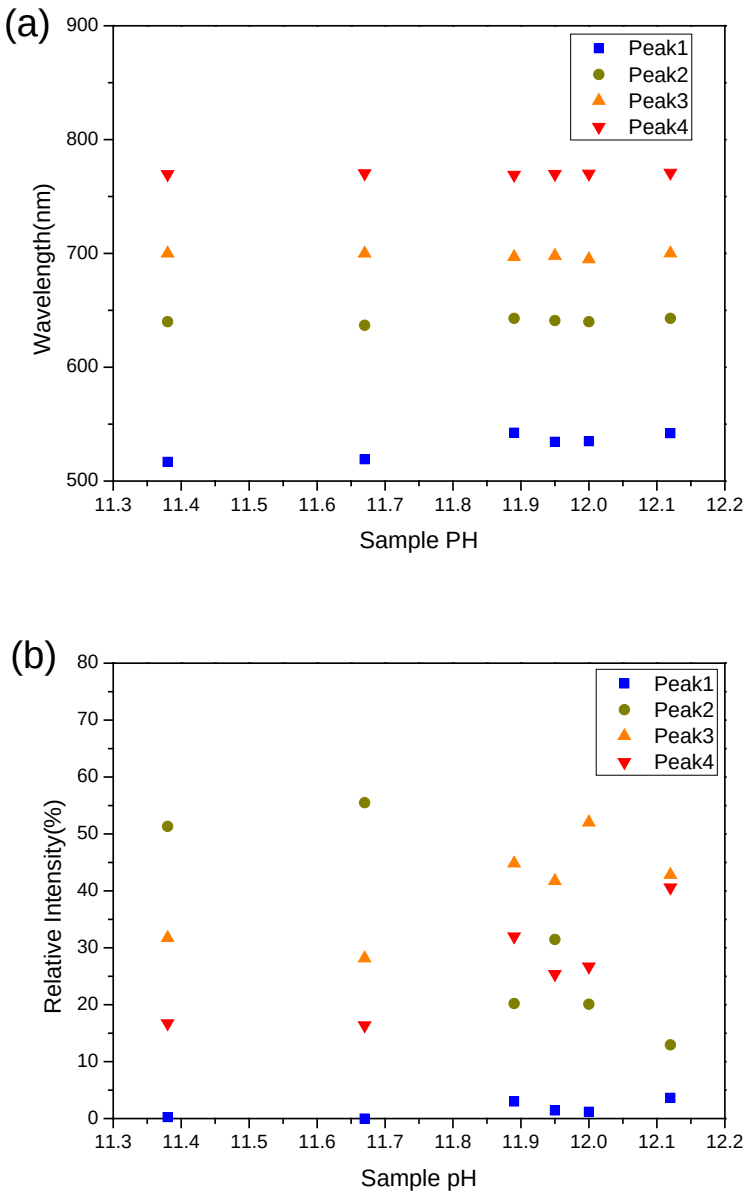

Figure 3.8 Peak location (a) and relative intensity (b) of fitted emission spectra of AuNCs with different pH.

Figure 3.8(a) illustrates the peak position distribution of all the fitted peaks with various pH. Although peak 1, whose wavelength is under 550nm, drift towards longer wavelength as the pH increases, the peak position of peak 2, 3 and 4 whose relative intensity are in dominance as shown in figure 3.8 (b) seems constant. As listed in table 3.2, the average peak position of peak 2, peak 3 and peak 4 are 640.6nm, 698.9nm, 770.3nm respectively with a standard deviation of 1.8nm, 1.9nm and 0.9nm. The light energy corresponding to these three peaks are 1.93eV, 1.77eV and 1. 61eV respectively. Figure 3.8 shows the relative intensity of all the fitted peaks. In

accordance to the culmination shift of the spectra which could be easily observed in figure 3.5, the relative intensity of shorter wavelength peak 2 (640.6nm) decreases while the longer wavelength peak 3 (698.9nm) and peak 4 (770.4nm) increases as the synthesis pH ascending.

Table 3.2 Dedicate fitting parameters for fluorescence emission spectra

pH			11.38	11.67	11.89	11.95	12	12.12	Average	STDEV
Peak1	Position	(nm)	516.8	519.1	542.5	534.5	535	542	530.8	12.6
	FWHM	(nm)	31.6	37.9	96	105	83	89		
	Relative	Intensity	0.2	0	3	1.4	1.2	3.6		
Peak2	Position	(nm)	640	636.8	642.9	641	640	642.9	640.6	1.8
	FWHM	(nm)	89.8	92.1	84.5	86.4	80	86.3		
	Relative	Intensity	51.3	55.5	20.2	31.5	20.1	12.9		
Peak3	Position	(nm)	700	700	697	698	695	700.1	698.9	1.9
	FWHM	(nm)	87.1	86	104.1	96.7	98.3	106.7		
	Relative	Intensity	31.7	28.2	44.8	41.8	52	42.8		
Peak4	Position	(nm)	769.5	770.3	769	769.8	770	770.8	770.3	0.9
	FWHM	(nm)	106.9	103.2	138.8	120.5	112.9	138.2		
	Relative	Intensity	16.7	16.4	32	25.4	26.7	40.6		

Peak 2 and Peak 3 with average apex wavelengths of 640.6nm and 698.9nm are consistent with previous fitting works which have the spectra fitted by two Gaussian functions with central wavelengths of 639.1nm and 704.1nm[47]. However peak 3 whose relative intensity would ascend dramatically with increasing pH has never been found in the fluorescence spectra of BSA Au25 nanoclusters before.

3.3 Fluorescence lifetime of BSA-AuNCs

The lifetime of a fluorephore provides supplementary information to the emission spectra in the understanding of the fluorephorence mechanism. It also provides a way to distinguish fluorephores with overlapping emission spectra and has been demonstrated a powerful tool in biosensing and bioimaging.

Lifetime decay curves of AuNCs with different pH have been measured using TCSPC technique under 488nm excitation. A Long Pass 590nm filter was used to stop scattering light as well as possible fluorescence from BSA. Typical lifetime

fluorescence decay curves of BSA-AuNCs with short and long tac range were shown in Fig. 3.9.

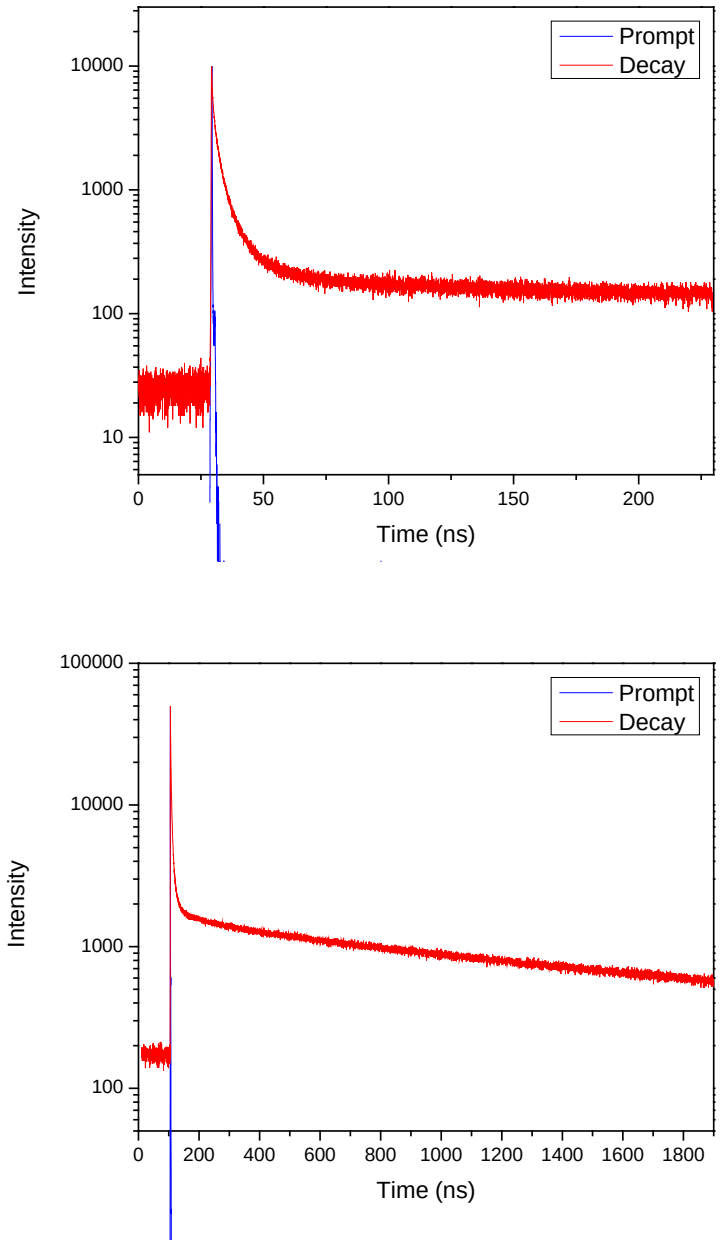

Figure 3.9 Lifetime decay curves of AuNCs using 488nm excitation with 200ns tac range (a) and 2us tac range (b).

Figure 3.9 suggests that the lifetime decay of BSA-AuNCs mainly consists of fast and slow decay components. These decay components are quite distinctive from the curve. So it would be easier and more accurate to fit them in two steps.

The fluorescence lifetime decay curve with a tag rang of 2us (right panel of figure 3.9) was fitted through following the two-steps process: first the long decay part (500ns to 2us) was fitted through a single exponential fitting and recorded as the long decay component; then a four exponential fitting on the whole decay curve was conducted with the last lifetime component fixed as the one obtained before. CHISQs of all the fits are below 1.05 which suggests the fitting should be acceptable. All four lifetime components and their relative intensity are listed in table 3.3.

It is found that among the four decay components, two short components have average lifetimes of 2.11ns and 7.48ns respectively, a mid decay compartment with an average lifetime of 87.74ns and a long component with an average lifetime of 1.10 μs. The lifetime distribution of two short nanosecond lifetime compartments and relative intensities of all lifetime compartments are shown in figure 3.10.

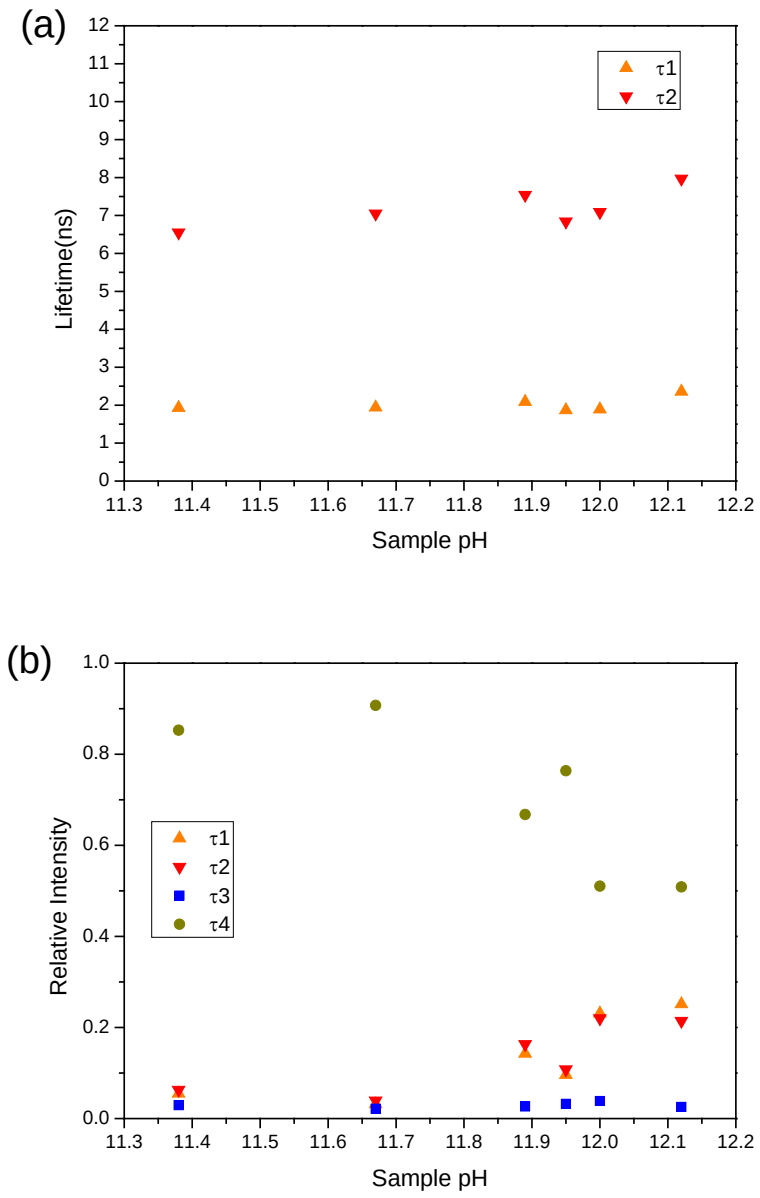

Figure 3.10 Lifetimes of two nanosecond lifetime components (a) and relative intensity of all four lifetime compoents (b) of AuNCs with different pH.

Table 3.3 Fitting parameters of lifetime decay

	τ_1 (ns)	Relative Intensity	τ_2 (ns)	Relative Intensity	τ_3 (ns)	Relative Intensity	τ_4 (μ s)	Relative Intensity
11.38	1.93	5.5	6.55	6.3	77.40	2.9	1.04	85.3
11.67	1.94	3.2	7.05	3.9	86.10	2.2	1.16	90.7
11.89	2.09	14.3	7.54	16.3	68.10	2.7	1.07	66.8
11.95	1.87	9.6	6.84	10.8	78.30	3.2	1.08	76.4
12.00	1.89	23.1	7.09	22.0	79.30	3.9	1.02	51.0
12.12	2.36	25.1	7.97	21.4	102.90	2.6	1.09	50.9
Average	2.11		7.48		87.74		1.10	
STDEV	0.17		0.52		15.89		0.04	

The two ns range lifetime components (as shown in figure 3.10 (a)) and the μs range long lifetime component are rather stable with different pH, while the mid decay component only contributes a small part to the total fluorescence intensity.

The lifetimes of the two short decay components, 2.11±0.17ns and 7.48±0.52ns, are comparable to the previously reported fast decay component of BSA protected Au25 (1.20ns and 5.27ns – 7.88ns with different excitation wavelength[27]). The long decay component found here slightly differs from the reported lifetime (1.10 μ s vs. 1.55 μ s) but is still in the same scale. The mechanism of the long decay component is still unclear. A model based on delayed fluorescence has been proposed to explain this slow decay process as discussed in the previous section 1.2.3 (fig. 1.12).

It can be seen from figure 3.10 (b) that the relative intensities of the two short lifetime components and the long component vary as the pH changes in contrast to the mid lifetime component. In addition, at pH above 11.7, the relatively intensities of short decay components increase as the pH increases along with the decreases of long decay component.

3.4 Growth Mechanism of BSA-AuNCs

Despite the advance in the synthesis and characterization of AuNC, study of the growth mechanism of nanoclusters still lags behind. In this work, a time lapse study was carried out to explore the growth mechanism of BSA-AuNCs, specifically, the influence of pH on the properties of the nanoclusters.

The experiment samples were prepared through the same method as the synthesis of normal BSA-AuNCs with pH 12.12 where 0.8mL of NaOH solution was added into the mixture. After 2 hours when the solution turned dark brown the first fluorescence emission spectrum, D0, was taken. The solution was then divided into two samples: S sample with additional HCl added to make a pH of 11.67 and R sample remained unchanged. Fluorescence spectra were taken from both samples in the following 20 days as shown in figure 3.11 with their peak position noted. The spectra of both series were fitted through the same method as in section 3.2.

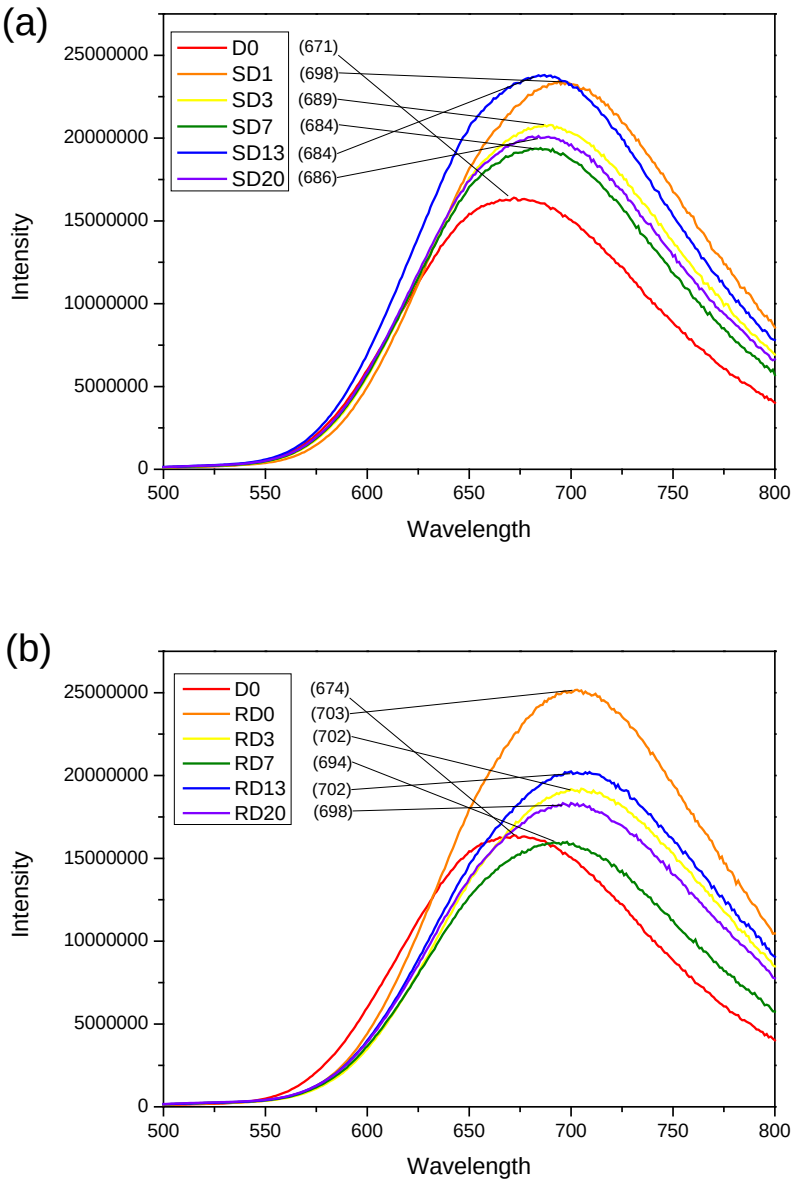

Figure 3.11 Fluorescence spectra of pH changed S series (a) and pH unchanged R series.

As illustrated in figure 3.11, the change of the fluorescence spectra with time is conspicuous. Figure 3.12 shows the evolution of emission peak positions of the two samples with time. It can be seen that, after the initial red shift during the first day for both samples, the emission peak of S sample blue shifted in the first week and maintained at ~686nm afterwards, while the original R sample didn't show much change in the following days. It is noted that the S sample has an emission close to that of the R sample (686nm vs. 698nm), but quite different from the sample that initially synthesized at pH 11.67 (650nm). It thus indicates that the optical properties of BSA-

AuNCs changed most distinctively at the first 2 hours of synthesis and gradually varying until day 7 when their emission became stable and ceased to change.

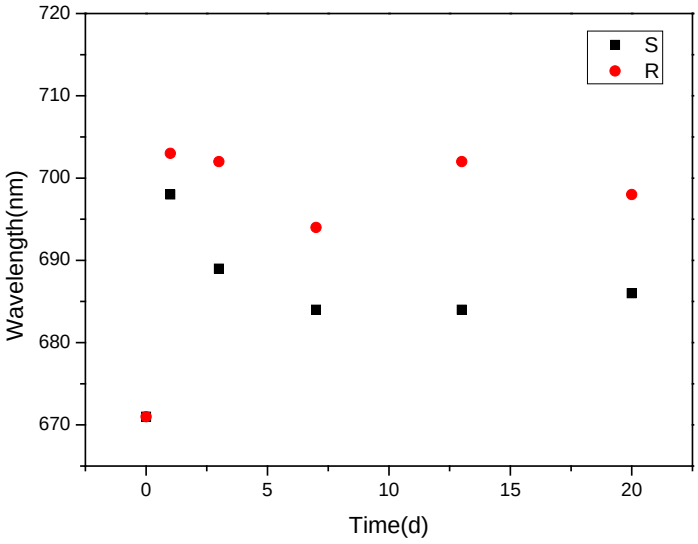

Figure 3.12 Emission peak position of S and R sample at different times.

This suggests that the growth of nanoclusters may consist of two stages: the formation of gold clusters with varies sizes/stabilities in the first stage followed by size focusing in the second stage which may take several days and eventually produce stable nanoclusters.

This is in line with a previous report that the quick reduction period would be completed within an hour[48] while the focusing process could last for days. Besides the influence on the reduction activity of BSA, pH could affect the focusing and size selection process. The fact that even with its pH tuned back to 11.67, the S sample does not have the same emission spectra as the one with the initial pH 11.67 indicates that pH affects the formation and size distribution of nanoclusters in the first 2 hours of the synthesis and its influence is not reversible in the following synthesis.

3.5 Mass Distribution of BSA Protected AuNCs

To study the size of gold nanoclusters, Matrix-Assisted Laser Desorption/ Ionization Time of Flight Mass Spectrometry (MALDI) has been employed to characterize the BSA-AuNCs prepared at PH 11.67 and 12.12. Before the measurement, both samples were purified to remove redundant ions using the following processes: first the pH of the solution was adjusted to isoelectric point 4.7 where BSA aggregated and became sediment; then the mixture was centrifuged to separate the sediment and solvent; finally the separated sediment was dissolved in distilled water at pH 11.0.

As shown in Fig. 3.13 (a), both spectra show 3 peaks. One is around 66kDa corresponding to pure BSA, with two other peaks centered at 70.4kDa and 72kDa corresponding to BSA-AuNCs. Previous mass spectroscopic study showed a single mass peak around 71kDa corresponding to BSA-Au_{25}.[17] Two peaks observed in this work suggest the formation of two types of BSA-AuNCs containing about 22 and 30 gold atoms respectively.

The purification process has little effect on the optical properties of the BSA-AuNCs. Figure 3.13 (b) shows the emission spectra of purified BSA-AuNCs samples and a clear disparity of the two emission peaks as observed before. However the mass spectra show no apparent difference, indicating a similar size distribution. Therefore the discrepancy in the emission spectra of BSA-AuNC synthesized at different pH is probably not due to the sizes of AuNCs and needs further investigation.

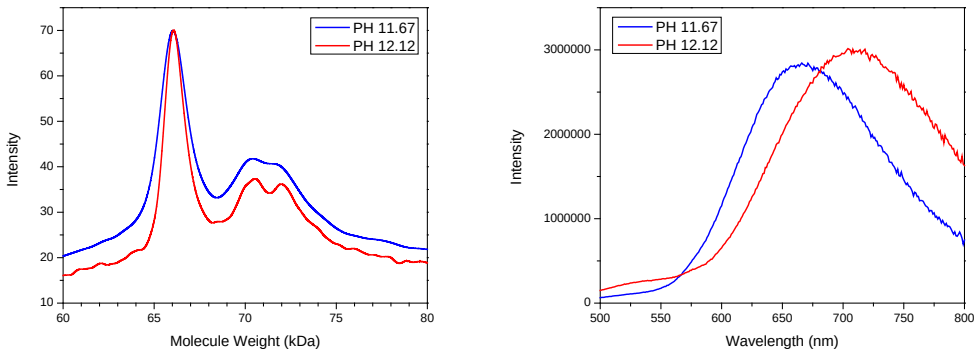

Figure 3.13 Mass (a) and fluorescence (b) spectra of AuNCs with pH of 11.67 and 12.12

3.6 Discussion and Conclusion

The pH during synthesis clearly has an influence on the optical properties of the BSA-AuNCs, in terms of both emission wavelength and fluorescence lifetime. Figure 3.14 shows the comparison between peaks intensity (a) and decay component intensity (b).

A simple fact which could be draw from figure 3.14 is that as the synthesis pH increases the intensity of the two longer wavelength fluorescence peaks, 698.9nm and 770.3nm, ascend while the shorter wavelength fluorescence peak, 640.6nm, descend. This corresponds to the increase of two short lifetime decay components, 2.11ns and 7.48ns, and decrease of long lifetime decay component, 1.10μs There are at least three different kinds of fluorescent emissions which either comes from different sources or different fluorescent mechanisms, in addition to the shortest wavelength peak (630.8nm) in fluorescence spectra with mid lifetime decay (87.74ns) in the lifetime curve.

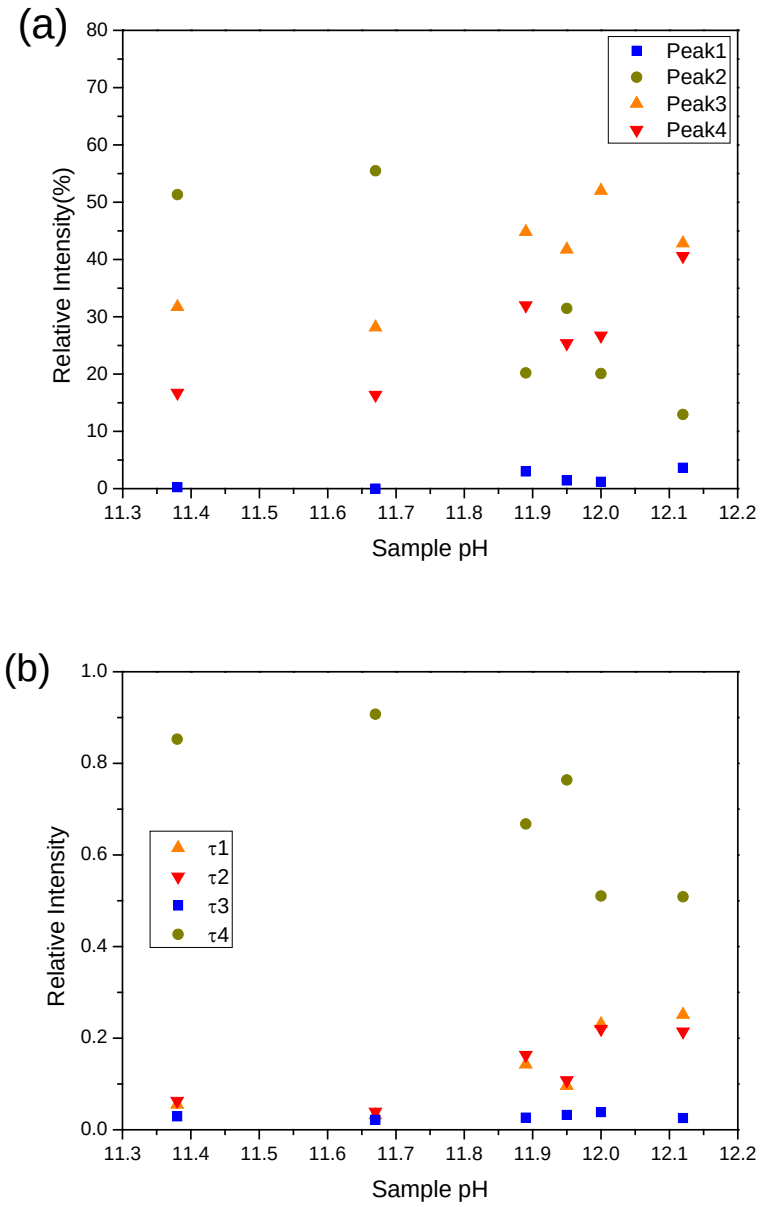

Figure 3.14 Comparison between peaks intensity (a) and decay components intensity (b)

The optical properties of nanoclusters depend on their structures[27] and surrounding electromagnetic environment[49], and pH could have an impact on both factors. The mass spectrometry study here indicates the existence of different kinds of nanoclusters, suggesting fluorescence emission might come from different sources although multiple fluorescence processes might be involved in each source. Further investigation is needed to reveal the fluorescence mechanism.

4. Applications of BSA-AuNCs in Biological Science

In an effort to eliminate the use of radioactive tracers, which are costly to use and dispose of, biosensing and bioimaging with fluorescence probes have drawn much research interest, which also provides possibilities for rapid and low-cost testing methods for a wide range of clinical, bioprocess, and environmental applications. BSA protected AuNCs have great potentials in biosciences for their attractive features including ultrasmall size, good biocompatibility and photostability, and tunable emission in the red to near-infrared spectral region.

4.1 Anisotropy Study on Glucose Oxidase linked BSA-AuNCs

With the intention of exploring the possibility of using fluorescent BSA-AuNCs in the study of protein-protein interactions, a series of experiments was performed on the study of the binding between glucose oxidase and BSA-AuNCs using an anisotropy measurement which prove to be a powerful and simple method to obtain information on the size and shape of fluorophores or rigidity of various molecular environments.[50,51]

4.1.1 Background

Glucose oxidase is an oxidoreductase that catalyses the oxidation of glucose to hydrogen peroxide and D-glucono-δ-lactone using molecular oxygen as an electron acceptor. It is widely used in the food and pharmaceutical industries[52] as well as a critical component in glucose biosensors.[53]

Figure 4.1 3D structure of glucose oxidase from aspergillus niger

Different kinds of glucose oxidase activity have been identified, however, the enzyme from Aspergillus niger has been biochemically characterized and used most extensively. Glucose Oxidase from Aspergillus niger is a homodimeric glycoprotein consisting of two equal subunits with a molecular mass of 80 kDa and each containing one tightly but noncovalently bound flavin adenine dinucleotide (FAD) cofactor per monomer where the glucose oxidase reaction take place. Figure 4.1 is a picture of 3D structure of glucose oxidase from aspergillus niger. [54]

The quantity of glucose oxidase is weighed by unit: one unit of glucose oxidase will oxidize 1.0 micromole of β-d-glucose to d-gluconic acid and hydrogen peroxide per minute at pH 5.1 at 35 ℃. Figure 4.2 is the schematic representation of the glucose oxidase reaction.

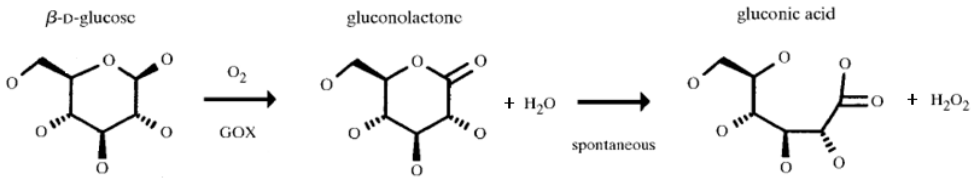

Figure 4.2 Schematic representation of the glucose oxidase reaction[54]

Glucose oxidase is also capable of forming glucose oxidase aggregates which are usually proposed as a means to immobilize glucose oxidase for glucose activity detection[55]. Several proteins could be used as proteic feeders in the formation of glucose oxidase aggregates among which BSA proved to have the highest immobilization efficiency[56]. It would be ideal to use glucose oxidase to test the

chemical activity of BSA within BSA-AuNCs to explore new possibility for utilizating fluorescent BSA-AuNCs in the study of protein-protein interactions.

4.1.2 Experimental

Glucose oxidase solution was prepared by dissolving glucose oxidase powder into PH 5.5 HCl buffer solution whose pH is optimised for glucose oxidase and its concentration measured through absorption spectrum. This glucose oxidase solution was added into as-prepared undiluted BSA-AuNCs solution (BSA concentration 25mg/ml) whose PH was also adjusted to 5.5 in a rate of one unit to 1uM which is suitable for cross-linking of BSA and glucose oxidase .[56] After half an hour in an ultrasonic bath, the mixture was incubated at 37 ˚C for about 12 hours. Then the anisotropy measurement was taken.

The same light source as in the lifetime measurement (488nm Delta Diode) was used to perform the anisotropy measurement, as well as the same filter (LP590). TAC range of the measurement was 100ns where clear anisotropy decay could be observed. G factors of the anisotropy were obtained right after the measurement using the same set up.

A single test of anisotropy measurement takes about 6 hours for the intensity of fluorescence is relatively low and repetition rate (100 kHz) is very low to avoid signal duplication. The temperature of the sample was measured using a thermal couple before and after the anisotropy measurement.

As mentioned in section 1.1.4, the rotation of fluorophores would obey Stokes-Einstein relationship if the flow in the solution is mainly laminar flow which usually is described by a non-dimensional quantity called the Reynolds number (Re).

$$Re = vR\rho_m / \eta \tag{4.1}$$

Where v and R are the speed and radius of particles, ρ_m is the density of the solution, and η is the fluid's viscosity.

The Reynolds number is the rate of inertial term to frictional force in the solution. When Re is small, friction dominates. Stirring produces the least possible response, namely laminar flow, and the flow stops immediately after the external force stops. When Re is big, inertial effect dominates, friction is negligible, and the flow is turbulent.

Thermal energy can usually be used as the external force for maintaining speed $\left(v^2 = 3k_BT/m\right)$ in equation 4.1 where η, k_B and T indicates the viscosity of the solution, Boltzmann constant and absolute temperature respectively.

In the case of this experiment, the solvent is distilled water whose density and viscosity under room temperature are 1 kg/L and 928.6 uPAs respectively; the radius and weight of glucose oxidase aggregates are estimated to be 12nm and 150kDa respectively while the radius and weight of pure BSA-AuNCs are about 3.4nm and 70kDa.[57]

The Reynolds number of the anisotropy measurement of glucose oxidase aggregates and BSA-AuNCs are estimated to be Re = $0.220*10^{-2}$ and Re = $0.110*10^{-2}$ respectively from the estimated radius and weight above, which are both much smaller than 1. The result shows that the rotation of fluorophores in this experiment obeys the Stokes-Einstein relationship so that equation 1.16 could be applied to calculate the radius of the rotation fluorophores.

$$R = \left(\frac{3\phi T k_b}{4\pi\eta}\right)^{1/3} \tag{4.2}$$

4.1.3 Results and discussion

Figure 4.3 illustrated the raw data of anisotropy measurement (a) as well as its corresponding anisotropy decay curve (b) which was obtained through equation 2.3. The rotational correlation time φ obtained through the fitting of anisotropy could be used to calculate the radius of fluorophore by equation 4.2.

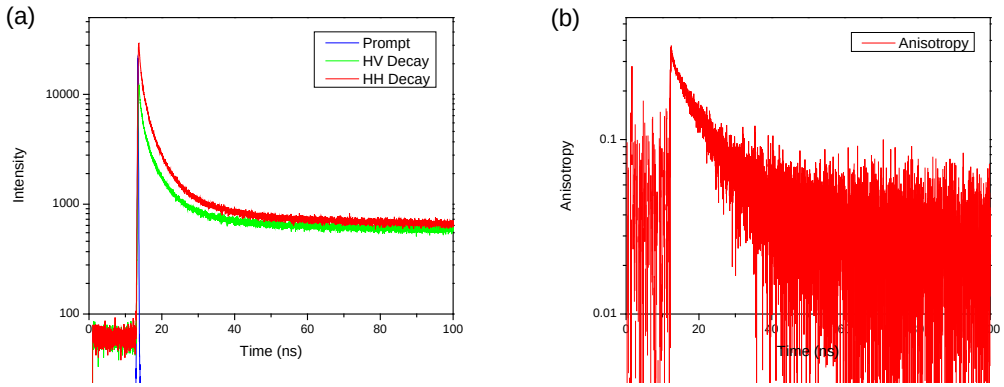

Figure 4.3 Anisotropy raw data(a) and anisotropy decay(b) of a typical anisotropy measurement

The radius of glucose oxidase – BSA-AuNCs and pure BSA-AuNCs calculated using equation 4.2 are listed in table 4.1 and shown in figure 4.4. Figure 4.4 also includes the radius of BSA-AuNCs from a series of anisotropy measurements taken at various temperatures by a colleague.

The calculated radius of BSA-Au25 is shorter than reported BSA radius from anisotropy measurement (about 3-4 nm)[57]. BSA has a heart-like shape (3nm*9nm*9nm)[58]. The discrepancy is likely due to the simplified spherical model used in calculation and other factors as discussed below.

Table 4.1 Fluorescence anisotropy of glucose oxidase linked AuNCs at different temperature

Sample NO.	Tem/K	η/uPAs	φ/us	R/nm
Sample 1	283	1322.5	1.89	11.01
Sample 1	296	928.6	2.54	13.87
Sample 1	308	709.1	1.57	13.10
Sample 1	320	577.8	1.49	13.96
Average				12.98
Sample 2	296	928.6	1.58	11.84
Sample 2	308	709.1	1.052	11.46
Average				11.65
Sample 3	296	928.6	1.78	12.32
Sample 3	310	682.4	1.32	12.55
Sample 3	283	1322.5	2.02	11.25
Sample 3	328	515.3	1.27	13.86
Sample 3	327	522.6	1.37	14.14
Average				12.82
BSA-Au25	293	1003.0	0.018	2.59

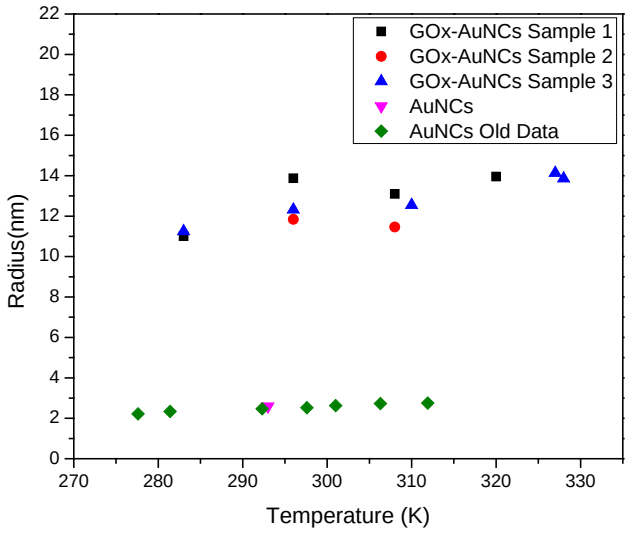

Figure 4.4 Anisotropy measurement results of glucose oxidase linked AuNCs and AuNCs at different temperature

Nevertheless, the glucose oxidase combined BSA-Au25 has a much larger radius (about 13nm) than that of BSA-Au25, showing that BSA-AuNCs was obviously linked

to glucose oxidase. This observation indicates that BSA in BSA-AuNCs remains its biochemical activity to participate in protein-protein interactions.

The anisotropy decay time of the glucose oxidase linked AuNCs is relatively long (about 2 us). It is usually very difficult or even impossible to measure the anisotropy decay as the fluorescence of the fluorephores would die out long before such long anisotropy decay. Luckily, the fluorescence lifetime of BSA-Au25 is also quite long (with average of 1.1 us). An Anisotropy measurement is meaningful when the fluorescence lifetime of the fluorephores and the lifetime of its anisotropy decay are comparable.

However, there're still some assumption and simplification within the data analysis. One is viscosity: the calculation was performed using the viscosity of water instead of the solution containing large amount of protein and ions. Using a viscosity lower than the actual viscosity would ended up with a larger radius as showed in Equation 4.2. Another problem is that the influence of temperature on the protein conformation was not been taken into account, though both BSA and glucose oxidase are stable under 333K, their structure might change as the temperature varies. The slight rising in radius as temperature increases might be the effect of protein structure variation.

4.2 Applications of BSA-AuNCs in Bioimaging

A study on drug delivery was performed using AuNCs as fluorescent labels. Drug vehicles loaded with BSA-AuNCs were feed into living rats directly as a fluorescence tracer to track the digestion and absorption of the drug within a living entity.

4.2.1 Sample preparation

The samples used in this study were prepared from rats intestine frozen sections. The samples were prepared through following processes[59]: First, Au NCs were loaded to lipid nanoparticls (bilosomes) then fed by oral gavages to adult rats; after 2 to 3 hours, parts of the upper intestine were collected and washed with phosphate buffer solution, then they were made into frozen sections(20 um section); at last the samples were counterstained by applying a drop of Vectashield mounting medium with DAPI so that the nucleus were stained with blue fluorescence.

4.2.2 Results and analysis

Figure 4.5, figure 4.6 and figure 4.7 shows the typical fluorescence microscopy images of samples from rats fed with nothing, BSA-AuNCs only and bilosomes loaded with BSA-AuNCs, separately. Images (c) in each figures were taken using 800nm excitation and a BP 435-485 filter. The blue areas in these images depict the fluorescence from DAPI that was excited under two photon excitation with an emission around 461nm. Blue oval-shaped patterns are typical cell nuclei (stained by DAPI) of rat intestine cells.

Images (b) (at the up right corner of each figures) were taken with excitation of 488 nm and a LP 505 filter. Wavelength of fluorescence from AuNCs is around 700nm. So if AuNCs do exists, their emissions should be observed in red in these images.

Besides AuNCs, some proteins and polysaccharides in cells may also have fluorescence in a similar emission band. However a distinct difference can be observed between figure 4.5 (b) and 4.6 (b): in figure 4.6 shows several very bright red spots while figure 4.5 doesn't have bright red features. We believe these red spots should be the aggregators of AuNCs. This suggests that BSA protected AuNCs can be absorbed by rats' intestine directly while still preserve its fluorescence, showing a great potential of BSA-AuNCs in the area of bioimaging. Figure 4.7 (b) shows bright red emission in the sample but no red spots as found in fig. 4.6 (b), suggesting that BSA-AuNC delivered via bilosomes were well distributed and there were no large aggregators formed. As the existence of autofluorescence background from cells, further study, e.g., fluorescence lifetime imaging utilization, is required for the quantitative analysis.

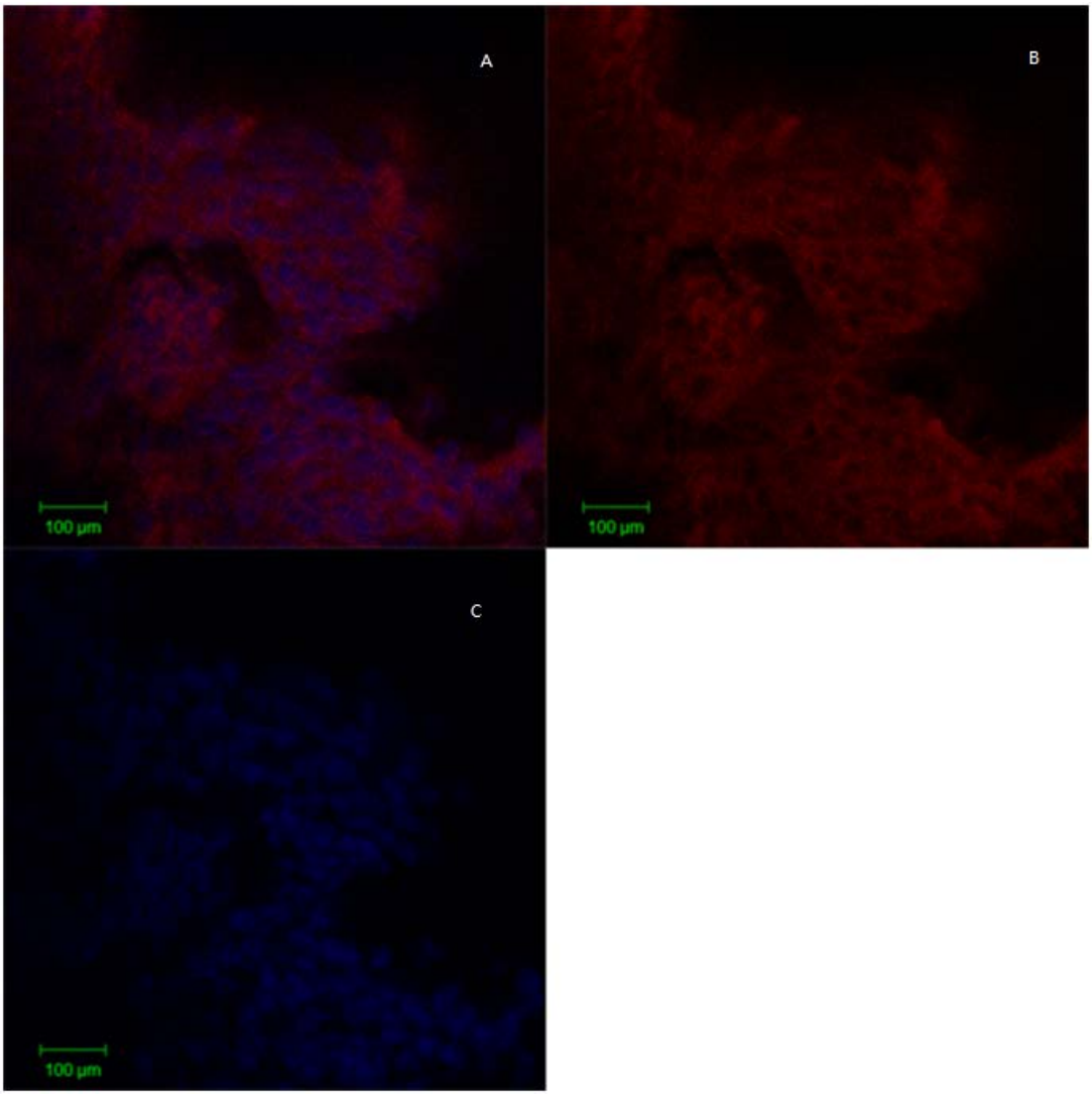

Figure 4.5 Fluorescence microscopy images of reference sample (Sample 1), (a)Combined figure of b and c(b)Fluorescence image with excitation of 488 nm and a LP 505 filter (c) using 800nm excitation and a BP 435-485 filter

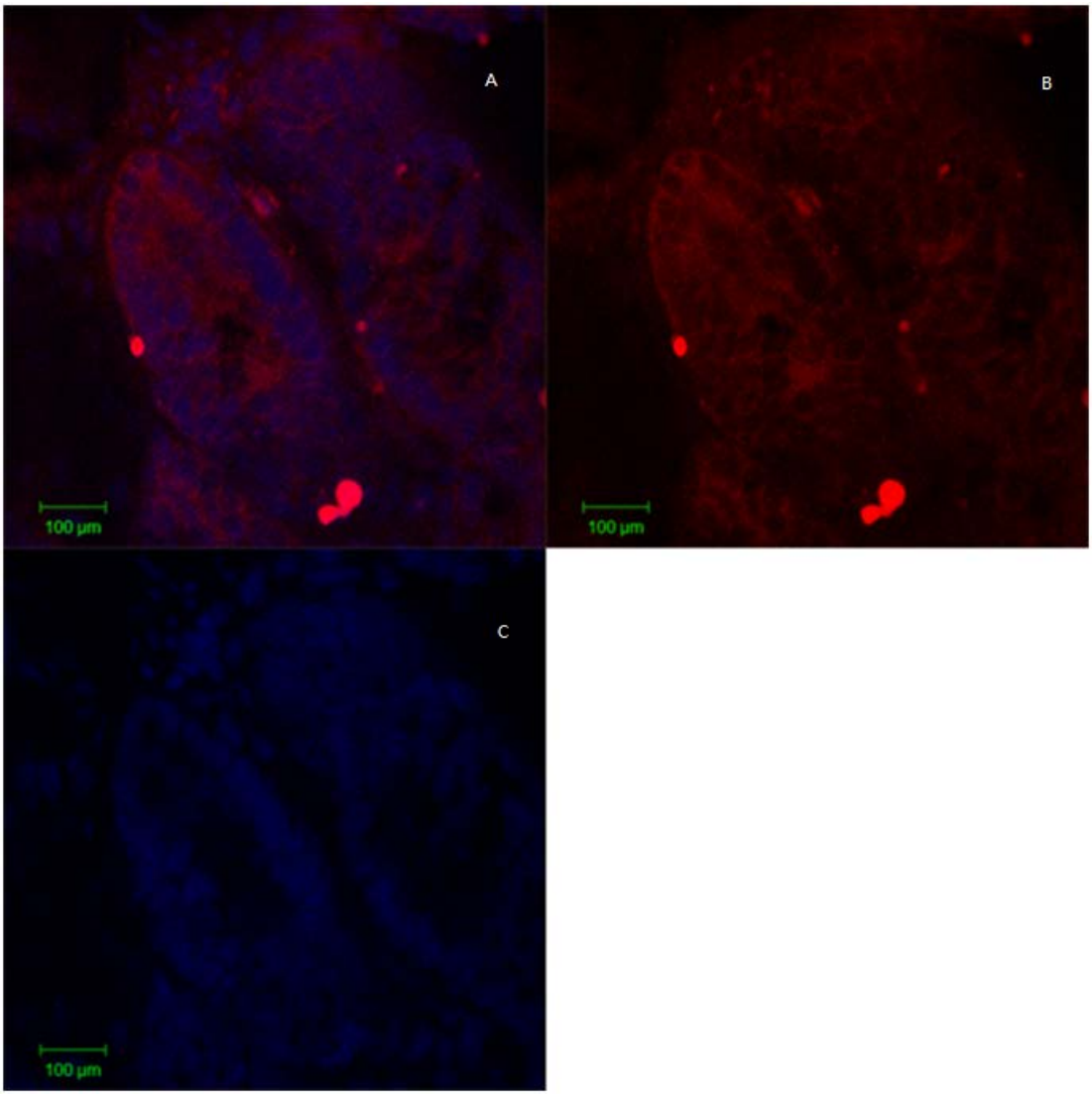

Figure 4.6 Microscopy Picture of Rats Fed with AuNCs Sample(Sample 2) (a)Combined figure of b and c(b)Fluorescence image with excitation of 488 nm and a LP 505 filter (c) using 800nm excitation and a BP 435-485 filter

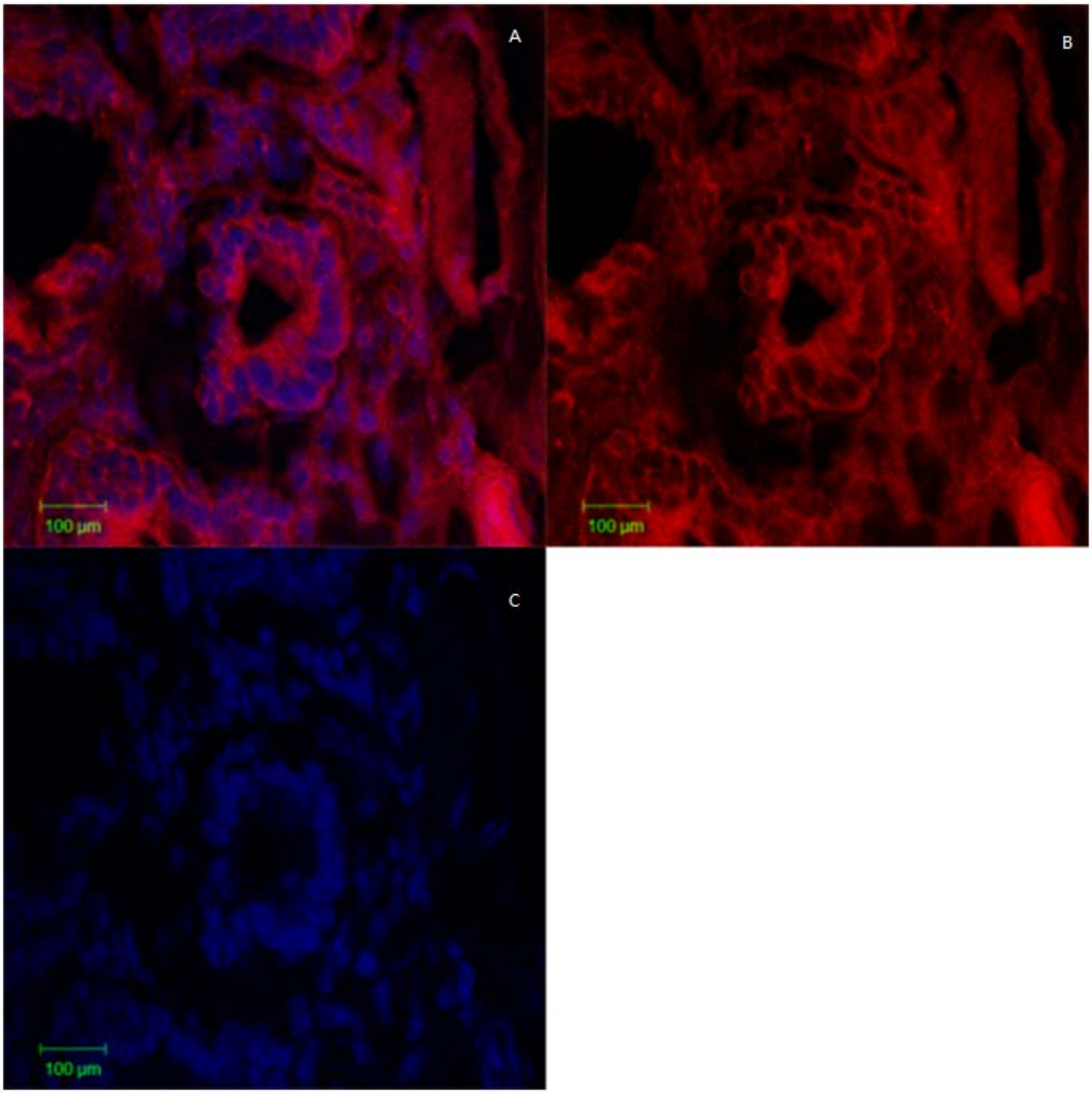

Figure 4.7 Confocal Microscopy Picture of Rats Fed with AuNCs and Drugs Sample(Sample 3) (a)Combined figure of b and c (b)Fluorescence image with excitation of 488 nm and a LP 505 filter (c) using 800nm excitation and a BP 435-485 filter

The images (a) combine image (b) and (c), providing an overlap mapping of blue and red emission that can be used to locate the BSA-AuNCs. Despite some cells are stack together in some areas, the images show BSA-AuNCs locating outside the nuclei areas as expected. Multiple images taken at different areas of each samples show similar features.

4.3 Conclusions

Studies in this chapter explored new application directions for BSA-AuNCs. Fluorescence anisotropy study on the glucose oxidase linked BSA-AuNCs could be developed into a novel glucose sensing technique which might be able to monitor glucose level without damaging the normal functions of organisms. And the studies on the “drug” (BSA-AuNCs) delivery via bilosomes and imaging of rats’ intestine samples showed that BSA-AuNCs could be used not only in cell studies but also in living animals.

5. Summary and Outlook

As a novel fluorescent nanomaterial, fluorescent AuNCs possess numerous exceptional characteristics compared with other luminescent materials such as good water-solubility, high photostability, large Stokes shift, ultrasmall size, nontoxicity, and good biocompatibility. This study focused on the optical properties and biological applications of BSA capped AuNCs.

In the AuNCs' optical property study, both the fluorescence emission and lifetime of AuNCs have been investigated and both are proved to be affected by the synthetic pH, and the fluorescence of the AuNCs are found to be composed of several components as the intensity of fluorescence emission and lifetime components share the same variation trend as the synthetic pH changes. Mass spectroscopy and kinetic fluorescence emission study also suggest the existence of different fluorescent components.

In order to understand the impact of synthetic pH on the optical properties of AuNCs as well as the relationship between the fluorescence emission and lifetime, more work should be carried out: a further study on the kinetic fluorescence during the synthesis of AuNCs might provide more information on the role that synthetic pH plays in AuNCs synthesis, and, lifetime decay of a certain narrow band would shed more light on the relationship between fluorescence emission and lifetime.

AuNCs are very attractive for biolabeling and bioimaging application with its ultrafine size and nontoxicity. Biological applications of AuNCs on both biosensing and bioimaging have been attempted in this work: the chemical activity of BSA of AuNCs has been confirmed through anisotropy study on the binding between glucose oxidase and AuNCs, and new utilization methods of AuNCs could be derived from this discovery. Moreover the bioimaging study opens a new possibility for this novel fluorescent material, and the long fluorescence lifetime of AuNCs makes it ideal for fluorescence lifetime imaging.

Acknowledgement

First and foremost, I would like to give my deepest gratitude to my supervisor Dr. Yu Chen, and Prof. David Birch who provided me valuable guidance in every stage of the writing procedure for this thesis. Their unselfish support, enlightening instruction, impressive kindness, patience and rigorous supervision helps a lot on this thesis. Their keen and vigorous academic observation enlightens me not only in this thesis but also in my future study.

I would like to extend my thanks to the academic staff: Olaf Rolinski, Jens Sutter, my colleagues: Philip Yip, Yinan Zhang, Peng Gu, Guoke Wei and Wenqin Li. These kind people have not only inspired me with their understandings on the subjects of nano-science, but also helped me with experimental settings. My sincere appreciation also goes to those kind technicians from the physics Department at the University of Strathclyde: Bob Dawson, Ged Drinkwater, and John Revie. I would not have gotten any results from cluster source without their patient technical support.

Last but not least, I'd like to thank my parents; I could not even start this project without their support and encouragement.

Reference

1. Lakowicz, J. *Principles of fluorescence spectroscopy*. (2009).

2. Pap, E. H. W., ter Horst, J. J., van Hoek, A. & Visser, A. J. W. G. Fluorescence dynamics of diphenyl-1,3,5-hexatriene-labeled phospholipids in bilayer membranes. *Biophys. Chem.* **48,** 337–351 (1994).

3. Mazza, M. G., Giovambattista, N., Stanley, H. E. & Starr, F. W. Dynamical heterogeneities and the breakdown of the Stokes-Einstein and Stokes-Einstein-Debye relations in simulated water. *Phys. Rev. E - Stat. Nonlinear Soft Matter Phys.* **76,** 031203 (2007).

4. Zheng, J., Nicovich, P. R. & Dickson, R. M. Highly Fluorescent Noble Metal Quantum Dots. *Annu. Rev. Phys. Chem.* **22,** 4109 (2008).

5. Sardar, R., Funston, A. M., Mulvaney, P. & Murray, R. W. Gold nanoparticles: past, present, and future. *Langmuir* **25,** 13840–51 (2009).

6. Parker, J. F., Fields-Zinna, C. a & Murray, R. W. The story of a monodisperse gold nanoparticle: Au25L18. *Acc. Chem. Res.* **43,** 1289–96 (2010).

7. Harkness, K. M., Cliffel, D. E. & McLean, J. a. Characterization of thiolate-protected gold nanoparticles by mass spectrometry. *Analyst* **135,** 868–74 (2010).

8. Chaki, N. K., Negishi, Y., Tsunoyama, H., Shichibu, Y. & Tsukuda, T. Ubiquitous 8 and 29 kDa gold:alkanethiolate cluster compounds: mass-spectrometric determination of molecular formulas and structural implications. *J. Am. Chem. Soc.* **130,** 8608–10 (2008).

9. Le Guével, X., Daum, N. & Schneider, M. Synthesis and characterization of human transferrin-stabilized gold nanoclusters. *Nanotechnology* **22,** 275103 (2011).

10. Le Guevel, X. *et al.* Formation of Fluorescent Metal (Au, Ag) Nanoclusters Capped in Bovine Serum Albumin Followed by Fluorescence and Spectroscopy. *J. Phys. Chem. C* **115,** 10955–10963 (2011).

11. Negishi, Y., Nobusada, K. & Tsukuda, T. Glutathione-Protected Gold Clusters Revisited : Bridging the Gap between Gold (I) -Thiolate Complexes and Nanocrystals, Thiolate-protected Gold. *J. Am. Chem. Soc.* **127,** 5261–5270 (2005).

12. Chevrier, D. M., Chatt, A. & Zhang, P. Properties and applications of protein- stabilized fluorescent gold nanoclusters : short review. *J. Nanophotonics* **6,** 064504 (2012).

13. Qu, X. *et al.* Fluorescent Gold Nanoclusters : Synthesis and Recent Biological Application. *J. Nanomater.* **Article ID,** (2015).

14. Crookes-Goodson, W. J., Slocik, J. M. & Naik, R. R. Bio-directed synthesis and assembly of nanomaterials. *Chem. Soc. Rev.* **37,** 2403–12 (2008).

15. Yang, T., Li, Z., Wang, L., Guo, C. & Sun, Y. Synthesis, characterization, and self-assembly of protein lysozyme monolayer-stabilized gold nanoparticles. *Langmuir* **23(21),** 10533–10538 (2007).

16. Goswami, N., Saha, R. & Pal, S. K. Protein-assisted synthesis route of metal nanoparticles: exploration of key chemistry of the biomolecule. *J. Nanoparticle Res.* **13,** 5485–5495 (2011).

17. Xie, J., Zheng, Y. & Ying, J. Y. Protein-directed synthesis of highly fluorescent gold nanoclusters. *J. Am. Chem. Soc.* **131,** 888–889 (2009).

18. Wei, H. *et al.* Lysozyme-stabilized gold fluorescent cluster: Synthesis and application as Hg(2+) sensor. *Analyst* **135,** 1406–1410 (2010).

19. Xavier, P. L., Chaudhari, K., Verma, P. K., Pal, S. K. & Pradeep, T. Luminescent quantum clusters of gold in transferrin family protein, lactoferrin exhibiting FRET. *Nanoscale* **2,** 2769–76 (2010).

20. Kawasaki, H., Hamaguchi, K., Osaka, I. & Arakawa, R. ph-Dependent Synthesis of Pepsin-Mediated Gold Nanoclusters with Blue Green and Red Fluorescent Emission. *Adv. Funct. Mater.* **21,** 3508–3515 (2011).

21. Wen, F. *et al.* Horseradish peroxidase functionalized fluorescent gold nanoclusters for hydrogen peroxide sensing. *Anal. Chem.* **83,** 1193–6 (2011).

22. Tan, Y. N., Lee, J. Y. & Wang, D. I. C. Uncovering the design rules for peptide synthesis of metal nanoparticles. *J. Am. Chem. Soc.* **132,** 5677–86 (2010).

23. Luo, Z. *et al.* Toward understanding the growth mechanism: tracing all stable intermediate species from reduction of au(i)-thiolate complexes to evolution of au25 nanoclusters. *J. Am. Chem. Soc.* **136,** 10577–80 (2014).

24. Wilcoxon, J. P., Martin, J. E., Parsapour, F., Wiedenman, B. & Kelley, D. F. Photoluminescence from nanosize gold clusters. *J. Chem. Phys.* **108,** 9137 (1998).

25. Sakanaga, I. *et al.* Photoluminescence from Excited Energy Bands in Au25 Nanoclusters. *Appl. Phys. Express* **4,** 095001 (2011).

26. Zheng, J., Zhang, C. & Dickson, R. M. Highly fluorescent, water-soluble, size-tunable gold quantum dots. *Phys. Rev. Lett.* **93,** 077402 (2004).

27. Wen, X., Yu, P., Toh, Y. & Hsu, A. Fluorescence Dynamics in BSA-Protected Au25 Nanoclusters. *J. Phys. …* **116,** 19032–19038 (2012).

28. Zhu, M., Aikens, C. M., Hollander, F. J., Schatz, G. C. & Jin, R. Correlating the crystal structure of a thiol-protected Au25 cluster and optical properties. *J. Am. Chem. Soc.* **130,** 5883–5 (2008).

29. Wu, Z. & Jin, R. On the ligand's role in the fluorescence of gold nanoclusters. *Nano Lett.* **10,** 2568–73 (2010).

30. Link, S. *et al.* Visible to Infrared Luminescence from a 28-Atom Gold Cluster. *J. Phys. Chem. B* **106,** 3410–3415 (2002).

31. He, S. *et al.* Design of a gold nanoprobe for rapid and portable mercury detection with the naked eye. *Chem. Commun. (Camb).* **7345,** 4885–7 (2008).

32. Liu, C.-W., Hsieh, Y.-T., Huang, C.-C., Lin, Z.-H. & Chang, H.-T. Detection of mercury(II) based on Hg2+ -DNA complexes inducing the aggregation of gold nanoparticles. *Chem. Commun. (Camb).* 2242–4 (2008). doi:10.1039/b719856f

33. Xie, J., Zheng, Y. & Ying, J. Y. Highly selective and ultrasensitive detection of Hg(2+) based on fluorescence quenching of Au nanoclusters by Hg(2+)-Au(+) interactions. *Chem. Commun.* **46,** 961–963 (2010).

34. Guo, C. & Irudayaraj, J. Fluorescent Ag clusters via a protein-directed approach as a Hg(II) ion sensor. *Anal. Chem.* **83,** 2883–2889 (2011).

35. Lin, Y.-H. & Tseng, W.-L. Ultrasensitive sensing of Hg(2+) and CH(3)Hg(+) based on the fluorescence quenching of lysozyme type VI-stabilized gold nanoclusters. *Anal. Chem.* **82,** 9194–9200 (2010).

36. Hu, D., Sheng, Z., Gong, P., Zhang, P. & Cai, L. Highly selective fluorescent sensors for Hg(2+) based on bovine serum albumin-capped gold nanoclusters. *Analyst* **135,** 1411–6 (2010).

37. Liu, Y., Ai, K., Cheng, X., Huo, L. & Lu, L. Gold-Nanocluster-Based Fluorescent Sensors for Highly Sensitive and Selective Detection of Cyanide in Water. *Adv. Funct. Mater.* **20,** 951–956 (2010).

38. Lin, Z. *et al.* Recyclable fluorescent gold nanocluster membrane for visual sensing of copper(ii) ion in aqueous solution. *Analyst* **137,** 2394–2399 (2012).

39. Liu, H. *et al.* Rapid sonochemical synthesis of highly luminescent non-toxic AuNCs and Au@AgNCs and Cu (II) sensing. *Chem. Commun.* **47,** 4237–4239 (2011).

40. Durgadas, C. V, Sharma, C. P. & Sreenivasan, K. Fluorescent gold clusters as nanosensors for copper ions in live cells. *Analyst* **136,** 933–940 (2011).

41. Habeeb Muhammed, M. A. *et al.* Luminescent quantum clusters of gold in bulk by albumin-induced core etching of nanoparticles: metal ion sensing, metal-enhanced luminescence, and biolabeling. *Chemistry* **16,** 10103–12 (2010).

42. Retnakumari, A. *et al.* Molecular-receptor-specific, non-toxic, near-infrared-emitting Au cluster-protein nanoconjugates for targeted cancer imaging. *Nanotechnology* **21,** 055103 (2010).

43. Liu, C.-L. *et al.* Insulin-directed synthesis of fluorescent gold nanoclusters: preservation of insulin bioactivity and versatility in cell imaging. *Angew. Chem. Int. Ed. Engl.* **50,** 7056–60 (2011).

44. Li, D.-U. *et al.* Real-time fluorescence lifetime imaging system with a 32 x 32 0.13microm CMOS low dark-count single-photon avalanche diode array. *Opt. Express* **18,** 10257–10269 (2010).

45. Ghiran, I. C. Introduction to fluorescence microscopy. *Methods Mol. Biol.* **689,** 93–136 (2011).

46. Pawley, J. B. & Masters, B. R. Handbook of Biological Confocal Microscopy, Third Edition. *J. Biomed. Opt.* **13,** 029902 (2008).

47. Wen, X., Yu, P., Toh, Y. R. & Tang, J. Structure-correlated dual fluorescent bands in BSA-protected Au 25 nanoclusters. *J. Phys. Chem. C* **116,** 11830–11836 (2012).

48. David, C., Guillot, N., Shen, H., Toury, T. & De La Chapelle, M. L. SERS detection of biomolecules using lithographed nanoparticles towards a reproducible SERS biosensor. *Nanotechnology* **21,** 475501 (2010).

49. Wang, S., Zhu, X., Cao, T. & Zhu, M. A simple model for understanding the fluorescence behavior of Au25 nanoclusters. *Nanoscale* **6,** 5777–81 (2014).

50. Groza, R. C., Calvet, A. & Ryder, A. G. A fluorescence anisotropy method for measuring protein concentration in complex cell culture media. *Anal. Chim. Acta* **821,** 54–61 (2014).

51. Ameloot, M., VandeVen, M., Acuña, A. & Valeur, B. Fluorescence anisotropy measurements in solution: Methods and reference materials (IUPAC Technical Report). *Pure Appl. …* **85,** 589–608 (2013).

52. Fogarty, W. M. & Kelly, C. T. in *Microb. Enzym. Biotechnol.* 177–226 (1990).

53. De Oliveira, A. C. A., Assis, V. C., Matos, M. A. C. & Matos, R. C. Flow-injection system with glucose oxidase immobilized on a tubular reactor for determination of glucose in blood samples. *Anal. Chim. Acta* **535,** 213–217 (2005).

54. Wohlfahrt, G. *et al.* 1.8 and 1.9 A resolution structures of the Penicillium amagasakiense and Aspergillus niger glucose oxidases as a basis for modelling substrate complexes. *Acta Crystallogr. Sect. D Biol. Crystallogr.* **55,** 969–977 (1999).

55. Bankar, S. B., Bule, M. V., Singhal, R. S. & Ananthanarayan, L. Glucose oxidase - An overview. *Biotechnol. Adv.* **27,** 489–501 (2009).

56. Ispirli, Y. & Ayhan, H. Proteic Feeder Effect on Glucose Oxidase Aggregates Formation. *HACETTEPE J. Biol. Chem.* **36,** 313–318 (2008).

57. Flecha, F. L. G. & Levi, V. Determination of the molecular size of BSA by fluorescence anisotropy. *Biochem. Mol. Biol. Educ.* **31,** 319–322 (2003).

58. Lee, C. T., Smith, K. a & Hatton, T. A. Photocontrol of protein folding: the interaction of photosensitive surfactants with bovine serum albumin. *Biochemistry* **44,** 524–536 (2005).

59. Norris, G., Gebril, A., Ferro, V. a & McConnell, G. Methanol immersion reduces spherical aberration of water dipping lenses at long wavelengths used in multi-photon laser scanning microscopy. *Biomed. Opt. Express* **3,** 3314–24 (2012).